Master's thesis:

"Role of the Retromer Complex in Ferroptosis"

Author: Nurzhan Abdukarimov

ORCID ID: 0000-0003-0916-8718

Supervisor: Jeannette Kunz, PhD

Nazarbayev University School of Medicine

Department of Biomedical Sciences

Master of Molecular Medicine

April 2024

DECLARATION

I hereby declare that the thesis is my original work, and it has been written by me in its entirety. I have duly acknowledged all the sources of information, which have been used in the thesis. This thesis has also not been submitted for any degree in any university previously.

Student name: Nurzhan Abdukarimov

Signature: 

Acknowledgments

I sincerely thank my supervisor Dr. Jeannette Kunz for providing me with a fantastic research opportunity and overall experience and for her endless support and patience. I also want to express my gratitude to research assistants Medina Khamijan and Banu Batyrova for teaching me the lab techniques, helping me design the experiments, and always having my back. I also want to thank Aiman Jalmukhambetova for helping me obtain the MDA-MB-231 cells and teaching me the basics of cell culturing and Aigul Kussanova for assisting me with flow cytometry experiments. Last but not least, I would like to thank Mereke Satkanov for always being by my side in the most critical of moments, as well as helping out with the statistical analyses.

Table of Contents

List of Tables

List of Figures

Figure 8. Effect of erastin treatment on viability in MDA-MB-231 cells after 24 h incubation. The cell viability was assessed using the Alamar blue reagent. DMSO was used as a solvent control. NT - no treatment. Letters “a”, “b”, and “c” indicate statistically significant differences between treatment groups. There is no significant difference between groups labelled with the same letters. The statistical significance was determined using ordinary one-way ANOVA ($P<0.0001$). The normality of the data was assessed using the Shapiro-Wilk test. The significance between different samples was assessed using Tukey's multiple comparisons test.

Figure 9. Ferroptosis regulation pathway. Ferrostatin exerts its anti-ferroptotic effects downstream of erastin (adapted from Abdalkader et al., 2018).

Figure 10. Effects of erastin treatment on the morphology of MDA-MB-231 cells are prevented by Fer-1 pre-treatment. DMSO was used as a solvent control.

Figure 11. Live fluorescence staining images of untreated and 10 uL erastin-treated MDA-MB-231 cells. Left - bright field image. Middle - BODIPY C11 fluorescence. Right - DAPI fluorescence.

Figure 12. Flow cytometry density plots demonstrating the effects of 10 uM erastin treatment with and without 5 uM Fer-1 pre-treatment. DMSO was used as a solvent control. Higher values of the SYTOX Blue signal indicate decreased viability and increased cell death. Lower values of the BODIPY C11 indicate an increased level of lipid peroxidation. The signal was gated on the FSC-A vs. SSC-A plot around the major cell cluster to exclude cell debris. FSC-A - area of the forward scatter signal. SSC-A - area of the side scatter signal. The data was analyzed and plotted using the FCS Express software.

Figure 13. Live fluorescence staining images of untreated and 10 uL erastin-treated MDA-MB-231 cells. Left - bright field image. Middle - MitoSOX Red fluorescence. Right - DAPI fluorescence.

Figure 14. MDA-MB-231 cells after transfection with the SNX3-pEGFP plasmid. **A.** Around 40-50% of the cells 24 h post-transfection expressed GFP. **B.** By 48 h post-transfection, GFP-expressing cells started exhibiting round morphology, detaching, and dying.

Figure 15. Diagram of KN2.0 non-homology-mediated CRISPR knockout kit. A. The kit includes two pCas-Guide constructs, each with a different guide RNA sequence, and a linear donor. The linear donor contains genes for puromycin resistance and GFP. The linear donor can integrate into the site of Cas-generated cleavage in two directions. B. Cell passaging protocol after transfection suggested by the manufacturer.

Figure 16. Green fluorescence image of transfected cells at >90% confluency before total DNA isolation. Cells transfected with the gRNA1-containing construct **(A)** and the gRNA2-containing construct **(B)**.

Figure 17. Setup and results of PCR. **A.** Scheme of the locations of primers used for PCR. **B.** Agarose gel electrophoresis of the resulting PCR product. The yellow arrow points at the band indicating potential reverse integration of the donor **C.** Combinations of primers used for PCR.

Figure 18. Immunofluorescence staining of SNX3 in normal and gRNA-transfected MDA-MB-231 cells. Nuclei were visualized with DAPI (blue). SNX3 was visualized with a secondary antibody conjugated to AlexaFluor 647 Plus (red).

Figure 19. Immunofluorescence staining of TFRC in normal and gRNA-transfected MDA-MB-231 cells. Nuclei were visualized with DAPI (blue). TFRC was visualized with a secondary antibody conjugated to AlexaFluor 647 Plus (red).

Figure 20. Nonspecific binding of the anti-SNX3 and anti-TFRC antibodies during Western blot. HRP-conjugated secondary antibodies were used. The proteins were visualized using the ECL substrate.

Abbreviations

TFRC - transferrin receptor 1

SNX3 - sorting nexin 3

GPX4 - glutathione peroxidase 4

PUFA - polyunsaturated fatty acids

GSH - glutathione

ACSL4 - acyl-CoA synthetase long-chain family member 4

LPCAT3 - lysophosphatidylcholine acyltransferase 3

RT-qPCR - quantitative reverse transcription polymerase chain reaction

CRISPR - clustered regularly interspaced short palindromic repeats

GFP - green fluorescent protein

DMSO - dimethylsulfoxide

TNBC - triple-negative breast cancer

gRNA - guide RNA

Abstract

Ferroptosis is a recently discovered mechanism of regulated cell death that occurs due to the excessive peroxidation of plasma membrane lipids. This reaction depends on catalysis by intracellular ferrous iron (Fe2+) and is counteracted by antioxidant defense systems. Transferrin receptor 1 (TFRC) is an essential contributor to intracellular iron metabolism because it facilitates the import of extracellular iron. Unsurprisingly, the overexpression of TFRC is an accurate marker of ferroptosis. Recent findings highlight the potential involvement of TFRC recycling in ferroptosis regulation. In particular, sorting nexin 3 (SNX3), a component of the retromer complex responsible for retrograde trafficking of TFRC, has been implicated in ferroptosis-induced cardiomyopathy. This makes SNX3 a potential target for therapeutic intervention or a marker of ferroptosis sensitivity. SNX3 expression is correlated with increased iron burden and epithelial–mesenchymal transition in breast cancer patients. Therefore, we hypothesize that SNX3 could play a role in promoting cancer development by increasing the amount of intracellular iron. Moreover, SNX3 might also sensitize cancer cells to ferroptosis-inducing agents.

Introduction

1. Cell death

Cell death is a fundamental biological process inherent to all living organisms. In animals, it has diverse functions in development, homeostasis, and pathology. Cell death pathways can be broadly classified as accidental (ACD) or regulated cell death (RCD) pathways (Galluzzi et al., 2018). ACD is uncontrollable and occurs when cells are exposed to harsh conditions, such as toxic chemicals or mechanical stresses. It causes permanent cell injury and is characterized by organelle swelling, plasma membrane rupture, and the release of intracellular components into the surrounding environment. In contrast, RCD is tightly regulated by genetically programmed mechanisms.

The first discovered and most extensively characterized type of RCD is apoptosis (Kerr et al., 1972). Apoptosis plays a central role in embryonic development, maintenance of tissue equilibrium, disease, and ageing. It is also the body's primary mechanism for the controlled removal of unwanted or damaged cells. The morphology of apoptotic cells includes membrane blebbing, cell shrinkage, nuclear condensation, and the formation of apoptotic bodies (Galluzzi et al., 2018). The mechanism of apoptosis involves the action of proteolytic caspases. In contrast to RCD, it is tightly controlled and accurate, ensuring mostly nonimmunogenic and clean removal of cells.

Dysregulation of apoptosis leads to a variety of pathological conditions. Most notably, disruption of apoptosis is a necessary step in the development of cancer (Hanahan & Weinberg, 2000). Cancer cells rely on the suppression of apoptotic mechanisms to survive and proliferate. Consequently, controlled induction of apoptosis is a commonly used strategy for cancer treatment.

In recent decades, many discoveries have been made in relation to other kinds of RCD. Pathways such as ferroptosis, pyroptosis, and parthanatos occur in specific contexts and employ mechanisms distinct from apoptosis (Galluzzi et al., 2018). These new pathways have been implicated in many diseases, including neurodegenerative disorders, cardiomyopathy, autoimmune and infectious diseases, and cancer. These pathways offer new targets for therapeutic interventions.

Particularly in the context of cancer treatment, drugs targeting new types of RCD can help us overcome frequent cases of resistance to drugs that promote apoptosis.

2. Ferroptosis

Ferroptosis is a distinct mechanism of RCD that depends on iron, a process first characterized by Stockwell and his team in 2012 (Dixon et al., 2012). Unlike apoptosis, pyroptosis, and necroptosis, which are governed by genetically programmed cascades of protein interactions, ferroptosis operates through metabolic pathways. This form of cell death is marked by the accumulation of lethal lipid peroxides, leading to alterations in mitochondrial morphology and, ultimately, the breakdown of the plasma membrane. (Stockwell, 2022).

Mechanistically, ferroptosis involves the peroxidation of polyunsaturated fatty acid phospholipids (PUFAs) facilitated by redox-active iron (Fe^{2+}), which acts as a catalyst (Gaschler & Stockwell, 2017). The reaction of iron with endogenous hydrogen peroxide or superoxide, known as the Fenton reaction, produces highly reactive radicals (Gaschler & Stockwell, 2017). These radicals can initiate a self-propagating chain reaction, abstracting hydrogen atoms from membrane-localized PUFAs to create toxic lipid peroxides (Gaschler & Stockwell, 2017). Further progression of this reaction can be terminated upon the action of antioxidants, the cell's primary defence against oxidative damage, which work to scavenge radicals (Gaschler & Stockwell, 2017). Therefore, the balance between reactive oxygen species (ROS) production and antioxidant defence mechanisms determines whether a cell will undergo ferroptosis or survive (see Fig.1)

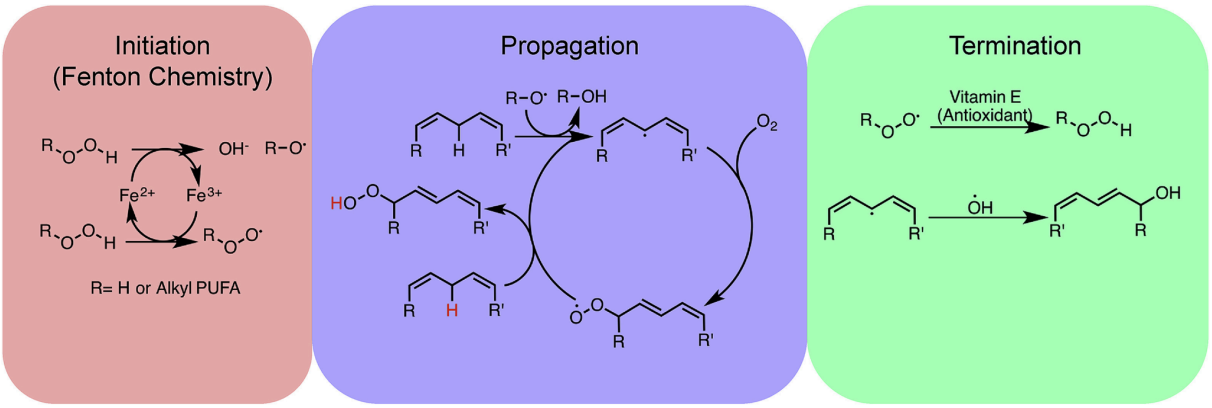

Figure 1. Mechanism of lipid peroxidation (adapted from Gaschler & Stockwell, 2017)

2.1. Ferroptosis and disease

Dysregulation of ferroptosis is linked to degenerative disorders such as Alzheimer's disease (AD), Parkinson's disease (PD), Huntington's disease (HD), and amyotrophic lateral sclerosis (ALS). Furthermore, it has been associated with complications arising in ischemia-reperfusion diseases of the kidney and heart, as well as autoimmune and infectious diseases (Amaral et al., 2019; Angelova et al., 2020; Bao et al., 2021; Friedmann Angeli et al., 2014; Hambright et al., 2017; P. Li et al., 2021; Sun et al., 2021; D. Wang et al., 2023; T. Wang et al., 2022). Conversely, the suppression of ferroptosis can contribute to tumorigenesis (Ubellacker et al., 2020; Yi et al., 2020). In fact, many types of cancers rely on antiferroptotic defence mechanisms to survive metabolic and oxidative stresses that are intrinsic to their distinctive biology (Lei et al., 2022). Therefore, developing therapeutic strategies that either induce ferroptosis in cancer cells or inhibit ferroptosis in other disorders holds considerable promise. However, realizing this potential requires substantial improvement in our understanding of the mechanisms of ferroptosis and the context in which it occurs.

2.2. The system Xc^-—GSH—GPX4 axis is the central regulator of ferroptosis

Ferroptosis inhibition is primarily carried out by the enzyme glutathione peroxidase 4 (GPX4) (Friedmann Angeli et al., 2014; W. S. Yang et al., 2014). It is capable of reducing toxic lipid hydroperoxides to nontoxic lipid alcohols (Brigelius-Flohé & Maiorino, 2013; Gaschler & Stockwell, 2017).

The function of GPX4 relies on the activity of an upstream cell membrane protein called the system Xc^- (Sato et al., 1999). The system Xc^- imports one molecule of cystine into the cell while exchanging it for one molecule of intracellular glutamate. The imported cystine molecule is then reduced to cysteine. Cysteine is in turn used for the synthesis of glutathione (GSH). Then, GPX4 employs GSH as a substrate for reducing lipid peroxides, a reaction that is unique even among glutathione peroxidases (Brigelius-Flohé & Maiorino, 2013).

Additionally, GPX4 was found to regulate the activity of lipoxygenases (LOXs) — enzymes that foster the peroxidation of PUFAs — underscoring the pivotal role of GPX4 as a key regulator of ferroptosis (Kühn & Borchert, 2002; Seiler et al., 2008).

Consequently, the inhibition of the system Xc^-—GSH—GPX4 axis represents a key event in the initiation of ferroptosis. For example, inhibition of the uptake of cystine, increased export of endogenous glutathione and upregulation of cysteine catabolism have all been shown to deplete GSH reserves and subsequently induce ferroptosis (Dixon et al., 2012; W. S. Yang et al., 2014). Similarly, inhibition of GPX4 — directly or by RNA interference — is capable of promoting ROS accumulation and subsequent ferroptosis (W. S. Yang et al., 2014).

On the other hand, maintaining the integrity and functionality of the system Xc^-—GSH—GPX4 axis is vital for ferroptosis evasion. This phenomenon is linked to drug resistance in cancers and diminished cell mortality in degenerative disease models (Banjac et al., 2008; L. Chen et al., 2022; Friedmann Angeli et al., 2019; Viswanathan et al., 2017).

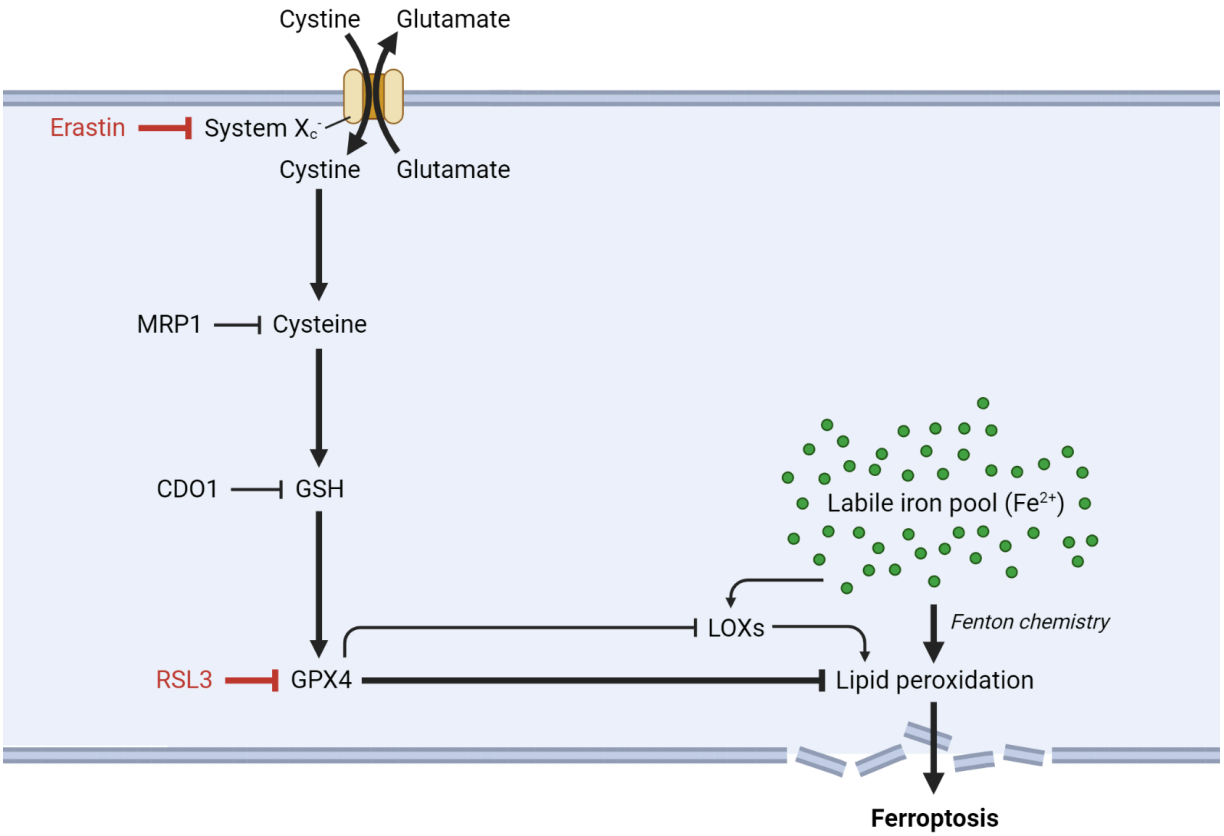

Figure 2. The system Xc^-—GSH—GPX4 axis negatively regulates ferroptosis by suppressing excessive peroxidation of phospholipids. Created using *BioRender.com*

2.3. Lipid metabolism generates drivers of ferroptosis

Execution of ferroptosis requires the peroxidation of membrane-localized PUFAs, a process that is enabled through the inhibition of GPX4 (Hadian & Stockwell, 2023; Stockwell, 2022). Nonetheless, the loss of GPX4 function alone is not sufficient for inducing lipid peroxidation and subsequent ferroptosis. The functions of two more enzymes, acyl-CoA synthetase long-chain family member 4 (ACSL4) and lysophosphatidylcholine acyltransferase 3 (LPCAT3) are critical for the onset of ferroptosis (Hashidate-Yoshida et al., 2015; Kagan et al., 2017; Kuwata et al., 2019). These two enzymes facilitate the remodelling of PUFAs to PUFA-containing phospholipids (PUFA-PLs) and their insertion into cellular membranes. Then, processed and integrated PUFA-PLs can be oxidized and form toxic lipid peroxides (see Fig. 3).

Functional ACSL4 and LPCAT3 were shown to be essential for the occurrence of ferroptosis in GPX4-deficient cells (Dixon et al., 2015). Consequently, the inhibition of either ACSL4 or LPCAT3 can result in ferroptosis resistance even in GPX4-deficient cells (Doll et al., 2017; Reed et al., 2022). On the other hand, the upregulation of ACSL4 has been associated with increased sensitivity to ferroptosis in a number of disease models (Cheng et al., 2020; L. Liu & Kang, 2022; Miao et al., 2022; Qu et al., 2021; Wu & Liu, 2021; Zhang et al., 2022).

Recent research identified that calcium-independent phospholipase A2β (iPLA2β) can independently suppress ferroptosis (Chen et al., 2021). It reduces lipid peroxidation by specifically hydrolyzing peroxidized phospholipid tails (Chen et al., 2021; Sun et al., 2021). This suggests that the execution of ferroptosis is driven specifically by membrane-incorporated lipid peroxides. For example, supplementing ACSL4-deficient cells with PUFA-PL peroxides — but not PUFA peroxides — significantly enhanced cell death from ferroptosis (Kagan et al., 2017).

To sum up, the processes of PUFA remodelling and incorporation into phospholipids generate PUFA-PLs, primary substrates of peroxidation in ferroptosis. The resulting membrane-localized lipid peroxides are the drivers of ferroptosis.

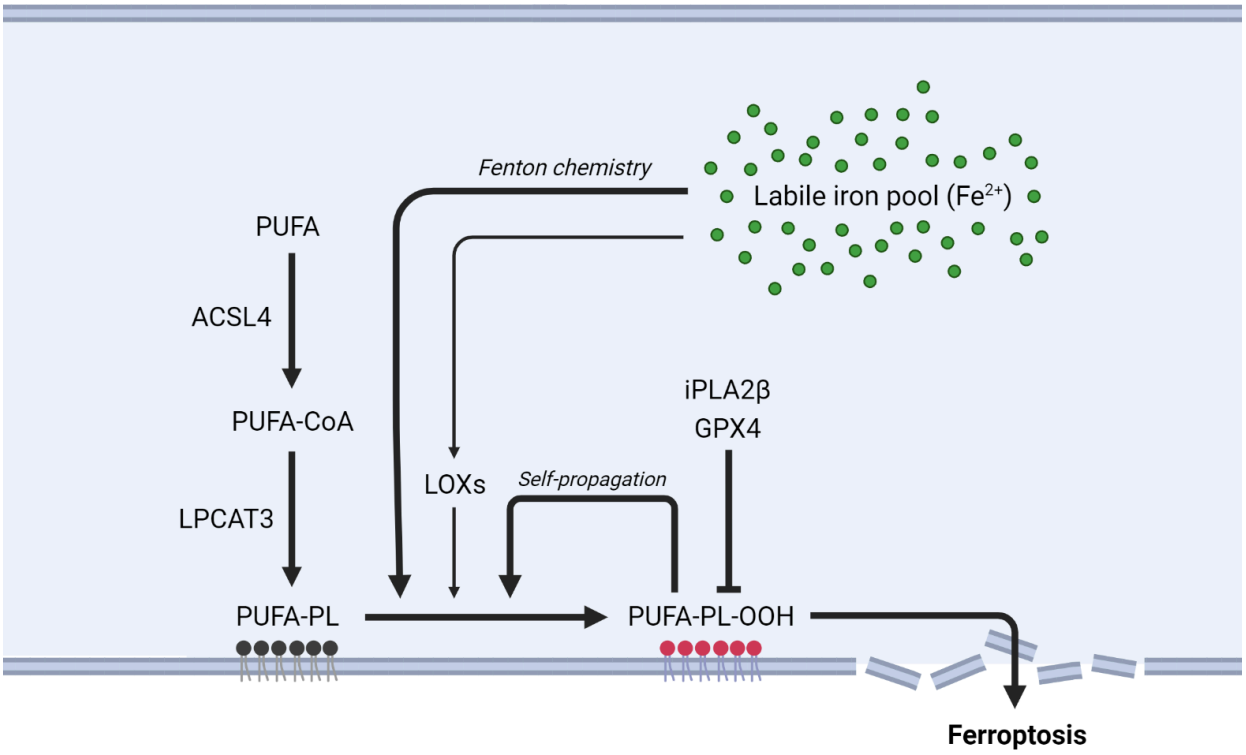

Figure 3. Lipid metabolism generates substrates for lipid peroxidation in ferroptosis. Created using *BioRender.com*

2.4. Role of iron metabolism and transferrin receptor in ferroptosis

The deposition of PUFAs onto cellular membranes and the impairment of antioxidant defences do not culminate in the generation of toxic lipid peroxides on their own. The initiation and progression of ferroptosis fundamentally rely on the accumulation of intracellular iron, hence the name of this death pathway (Stockwell, 2022). Excessive accumulation of intracellular iron has been linked to ferroptosis in studies of various diseases, including cardiomyopathy, multiple sclerosis, and diabetic osteoporosis among other disorders (Fang et al., 2019; Van San et al., 2023; Yang et al., 2022). Moreover, elevated iron load is intrinsic to many types of cancer, such as liver and breast cancers, presenting a significant vulnerability that is not typically targeted by apoptosis-inducing therapies (Chen et al., 2021; Hino et al., 2022; Pinnix et al., 2010).

Iron facilitates the oxidation of membrane-embedded PUFAs in several major ways: 1) by direct catalysis of the Fenton reaction by ferrous iron, and 2) by enabling enzymes such as LOXs, which contain iron, to catalyze the oxidation of PUFAs

(Dixon et al., 2012; Shah et al., 2018; Stockwell, 2022; W. S. Yang et al., 2016). Accordingly, the neutralization of redox-active iron using iron chelators can effectively inhibit ferroptotic cell death (Dixon et al., 2012; Kagan et al., 2017).

The intracellular metabolism of iron can roughly be categorized into import, storage, utilization, and export of iron. Recognition of extracellular iron and its entry into the cell is largely facilitated by the transferrin receptor 1 (TFRC) (Aisen, 2004). Iron in the blood is bound by transferrin, a natural chelating plasma protein, which can be bound by TFRC on the cell surface. The resulting transferrin-TFRC complex is then endocytically internalized via the clathrin-mediated mechanism. Within the endosome, the lower pH of the environment prompts iron (Fe^{3+}) to dissociate from transferrin. Then a ferrireductase STEAP3 colocalized on the endosomal membrane reduces released iron to Fe^{2+}. Subsequently, the divalent metal transporter 1 (DMT1), also present on the endosomal membrane, relocates Fe^{2+} into the cytosol (see Fig. 4) (Aisen, 2004; Ohgami et al., 2005). The TFRC and transferrin undergo recycling to return back to the cell surface.

Within the cell, iron can exist in the form of redox-active ferrous iron (Fe^{2+}) and contribute to the labile iron pool. However, it is mostly stored in a complex with ferritin, an iron-sequestering protein, due to labile iron's ability to induce oxidative stress (Arosio et al., 2009; Dixon & Stockwell, 2014). Excess ferrous iron can be removed through ferroportin, an intermembrane exporter of unbound iron, in addition to the sequestration by ferritin (Drakesmith et al., 2015). On the other hand, stored iron can be released when needed via the autophagy-dependent degradation of ferritin called ferritinophagy, as an additional source of ferrous iron besides the TFRC-mediated import (Mancias et al., 2014). These and other mechanisms of iron intake, storage, release, and export are carefully orchestrated by iron-regulatory proteins (IRPs) and determine the redox balance of the cell, and by extension, its susceptibility to ferroptosis (X. Chen et al., 2020; Feng et al., 2020; Gao et al., 2015; Hou et al., 2016; L. Li et al., 2018). As such, cellular iron metabolism can be modulated to selectively increase the susceptibility to ferroptosis in cancer or decrease it in the context of other diseases.

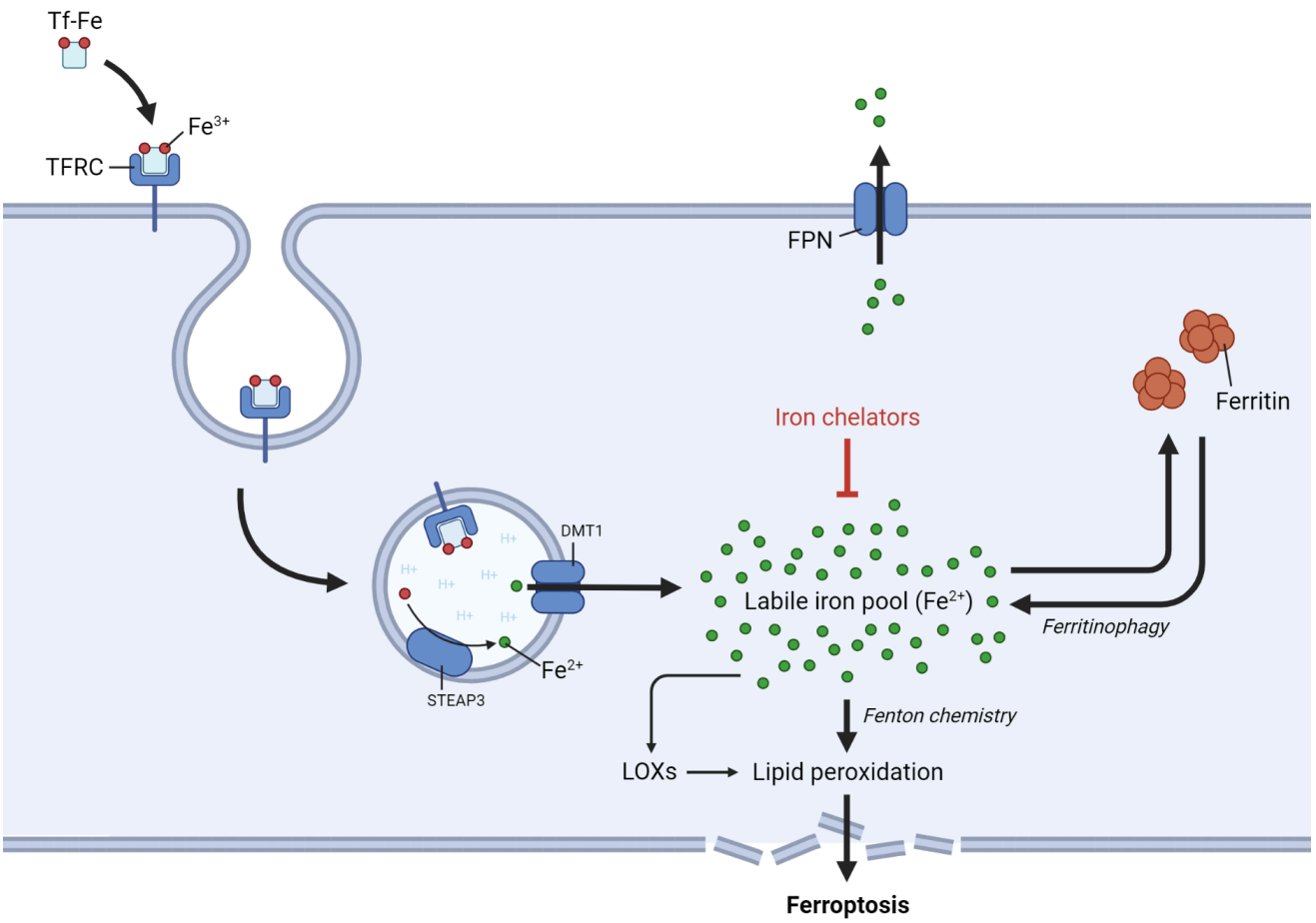

Figure 4. Iron metabolism facilitates lipid peroxidation in ferroptosis. Created using *BioRender.com*

3. Regulation of the iron metabolism by the retromer complex

Cells can regulate the intracellular concentration of iron in a number of ways. One of them is by decreasing or increasing the presence of TFRC on the surface of the plasma membrane, e.g., by altering the expression of TFRC. For instance, iron regulatory proteins (IRPs) can promote TFRC expression by stabilizing its mRNA (Anderson et al., 2012). Alternatively, the abundance of TFRC on the cell's surface can be affected by the activity of the endosomal sorting machinery.

When a cell surface receptor such as TFRC is endocytosed, it can either be recycled back to the plasma membrane or undergo lysosomal degradation (Cullen & Steinberg, 2018). The fate of the receptor is regulated in part by the retromer complex, a highly conserved complex of proteins VPS26, VPS29, and VPS35. This

complex can associate with different cargo adaptor proteins called sorting nexins (SNXs), which confer binding specificity to different internalized receptors.

The recycling of TFRC in particular is mediated by a complex of the retromer and sorting nexin 3 (SNX3) (C. Chen et al., 2013). SNX3-deficiency in red blood cells leads to the accumulation of TFRC in early endosomes, which hinders iron uptake and causes haemoglobin defects. The SNX3-retromer recognizes a sorting motif of TFRC, such as the Øx[L/M/V], in a pocket between SNX3 and VPS26 (Lucas et al., 2016). The binding of SNX3-retromer leads to membrane tubulation (Leneva et al., 2021). The resulting tubules undergo fission to produce cargo-transporting vesicles (see Fig. 5) (Cullen & Steinberg, 2018). Finally, TFRC-containing vesicles are directed to fuse with the plasma membrane by the exocyst complex (M. Chen et al., 2022). The lack of SNX3 signalling marks the receptor for degradation by default.

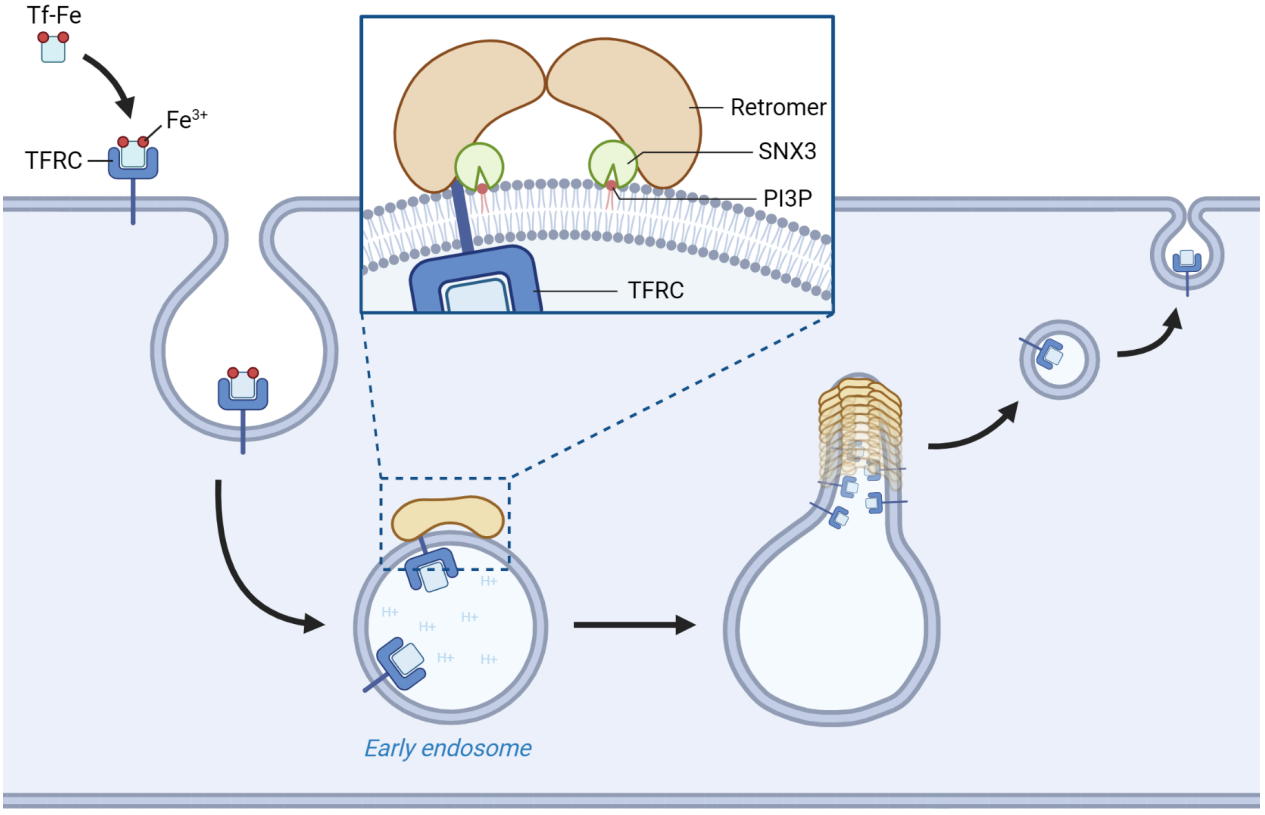

Figure 5. Recycling of TFRC to the membrane is mediated by SNX3. Created using *BioRender.com*

4. Role of SNX3 in ferroptosis

The accumulation of TFRC on the plasma membrane has been established as a very accurate marker of ferroptosis (Feng et al., 2020). This could not be explained by impaired internalization of the receptor. Therefore, it is possible that SNX3-mediated recycling of TFRC is involved in ferroptosis. Indeed, recent findings indicate that this exact mechanism is involved in doxorubicin-induced cardiomyopathy (Yu et al., 2023). It was demonstrated that the silencing of SNX3 alleviated Dox-induced cardiomyopathy. On the other hand, overexpression of SNX3 facilitated ferroptosis and exacerbated cardiomyopathy by increasing the recycling of TFRC to the plasma membrane.

This is an important implication for the development of cancer treatment as the expression of SNX3 could be correlated with susceptibility to ferroptosis. For example, in triple-negative breast cancer (TNBC) the expression of SNX3 is elevated (Öyken, 2020). Similarly, breast cancer typically has a significantly increased iron burden, possibly due to the SNX3-mediated recycling of TFRC. It is possible that higher iron levels may upregulate the function of some histone demethylases, and the initiation of subsequent epithelial-mesenchymal transition (EMT). This mechanism has been described for CD44, another protein implicated in importing extracellular iron (Müller et al., 2020). High expression of CD44 in breast cancer can lead to increased tumorigenesis and metastases (X. Liu et al., 2019). Interestingly, CD44 expression was shown to correlate with the expression of SNX3 in other models of cancer (Cingöz, 2019). SNX3 is known to regulate the retrograde transport of Wnt, which was also shown to regulate the activity of CD44 (Harterink et al., 2011; Walter et al., 2022). Therefore, SNX3 might promote iron accumulation required for cancer development via two distinct mechanisms, which at the same time might render cells more sensitive to ferroptosis induction. Still, details of the relationship between SNX3 expression, ferroptosis, and cancer progression remain unclear and require further investigation.

Hypothesis and aims

SNX3 is a protein that controls the recycling of TFRC, a receptor that imports extracellular iron. Recent findings suggest that SNX3 induces ferroptosis by increasing the recycling of TFRC. Both SNX3 and iron levels are elevated in breast cancer, suggesting increased sensitivity to drug-induced ferroptosis. The functional relation between SNX3 and ferroptosis in cancers remains to be elucidated. It is possible that the facilitation of iron uptake by SNX3 allows cancer progression and EMT. However, the excessive iron load associated with this process might render cells more sensitive to ferroptosis-inducing agents. Therefore, the expression of SNX3 might be a potential marker for ferroptosis sensitivity in tumors.

Hypothesis

We hypothesize that SNX3 might be involved in ferroptosis by promoting the recycling of TFRC, thus facilitating iron uptake in breast cancer cells (See Fig. 6).

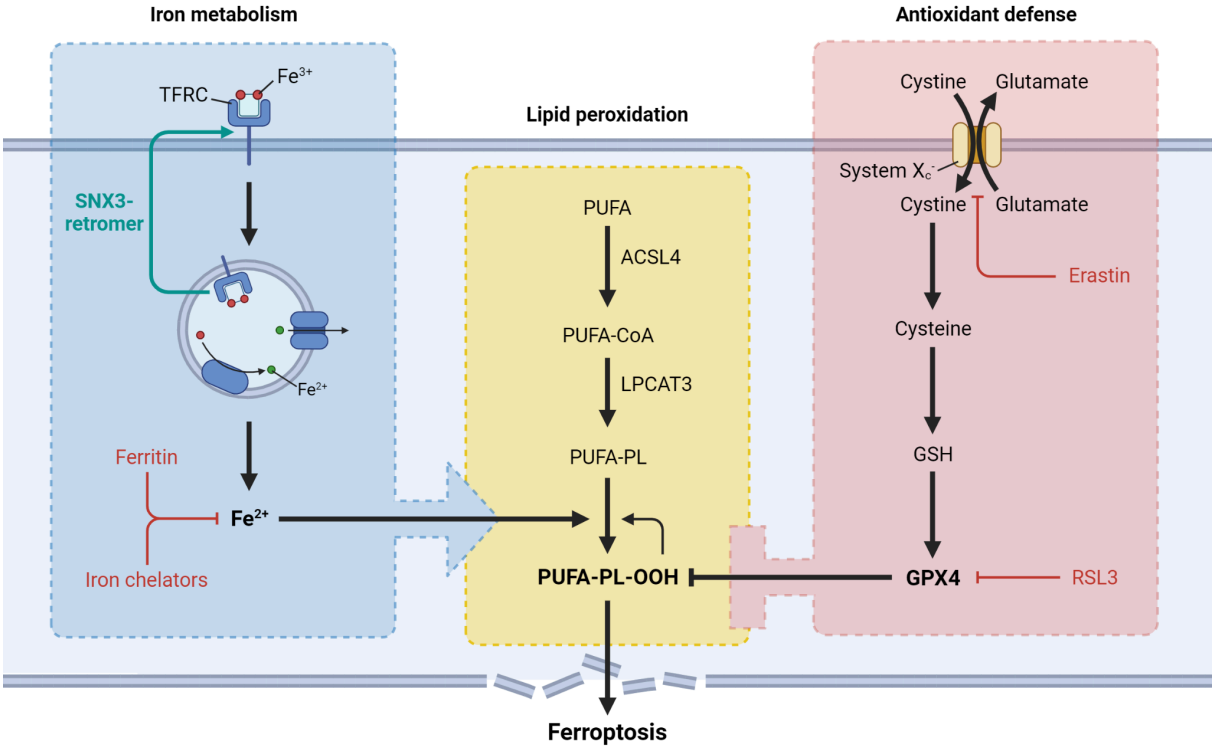

Figure 6. The hypothesized mechanism by which SNX3 is involved in ferroptosis. Created using *BioRender.com*

Aim

This project aims to investigate the relationship between the expression of SNX3 and the susceptibility of breast cancer cells to erastin-induced ferroptosis.

Objectives

To achieve the aim, the following objectives have been selected:

- Establish the effective concentrations of erastin
- Observe the effect of erastin treatment on cell viability, morphology, and signs of ferroptosis
- Produce breast cancer cell lines with varying levels of SNX3 via overexpression and knockout
- Investigate the relationship between levels of SNX3 expression and susceptibility to ferroptosis by flow cytometry
- Investigate the relationship between SNX3 expression and TFRC expression
- Investigate whether SNX3 could be involved in ferroptosis induction via direct association with TFRC

Materials and Methods

Table 1. List of reagents used

Material	**Description**
Cell culture medium	Gibco DMEM, high glucose, GlutaMAX (cat. #10566016) with 10% Gibco FBS (cat. #16000044), 1% Gibco Penicillin-Streptomycin (cat. #15140122), and 1% Cytiva HyClone Non-Essential Amino Acids (cat. #11591861)
1X PBS	Prepared from ChemCruz Phosphate Buffered Saline: 500 ml of 10X (cat. #sc-362298)
Trypsin 0.25 % - EDTA	Aliquoted from Trypsin 0.25 % - EDTA in HBSS w/o Calcium w/o Magnesium w/ Phenol Red (cat. #L0931) and stored at -20°C long-term, +4°C short-term.
DMSO	Pierce Dimethylsulfoxide (DMSO), Sequencing Grade (cat. #20688)
Cell freezing medium	Plain Gibco DMEM with 20% FBS and 10% DMSO
10X Running buffer	29 g of Trizma base (cat. #T1503-500G), 144 g of Glycine (cat. #1610718), and 10 g of SDS (Sodium Dodecyl Sulfate) (cat. #1610301) dissolved in 1 L of deionized water. 12N HCl was used to adjust the final pH to 8.3
10X Transfer buffer	3.03 g of Trizma base and 14.4 g of glycine dissolved in 500 mL deionized water and 200 mL pure methanol. The final volume was adjusted to 1 L with deionized water
10X Tris Buffered Saline (TBS)	24 g of Trizma base and 88 g of NaCl (cat. #S9625-1KG) dissolved in 900 mL of deionized water. 12N HCl was used to adjust the pH to 7.6. The final volume was adjusted to 1 L with deionized water
1X Tris Buffered Saline with Tween 20 (TBST)	100 mL of 10X TBST and 1 mL of Tween 20 (Cat. #9005-64-5)
Blocking buffer (3% BSA)	3 g of Bovine Serum Albumin (cat. #A4503-100G) dissolved in 100 mL of 1X TBST
1.5M Tris-HCl, pH 8.8	9.1 g of Trizma base dissolved in 50 mL deionized water. 12N HCl was used to adjust the final pH to 8.8

0.5M Tris-HCl, pH 6.8	3 g of Trizma base dissolved in 50 mL deionized water. 12N HCl was used to adjust the final pH to 6.8
10% SDS	5 g of SDS dissolved in 50 mL of deionized water
10% Ammonium persulfate (APS)	5 g of Ammonium persulfate, 98+% (cat. #401165000)
TEMED	N,N,N',N'-Tetramethylethylenediamine, Electrophoresis Grade (cat. #J63734.AC)
12% separating gel	6 mL 30% Acrylamide/Bis Solution 29:1 (cat. #1610156), 3.75 mL 1.5M Tris-HCl, pH 8.8, 150 uL 10% SDS, 75 uL 10% APS, 5.03 mL deionized water, 7.5 uL TEMED
4% stacking gel	1.98 mL 30% Acrylamide/Bis Solution 29:1, 3.78 mL 0.5M Tris-HCl, pH 6.8 150 uL 10% SDS, 75 uL 10% APS, 9 mL deionized water, 15 uL TEMED
1X RIPA buffer	Prepared from 10X RIPA Lysis Buffer (cat. #20-188) with the addition of 1% Halt Protease Inhibitor Cocktail (100X) (cat. #78429)
Loading buffer	1 volume of Laemmli SDS sample buffer, reducing (6X) (cat. #AAJ61337AD) was added to 5 volumes of total protein sample before loading to the gel
Pierce BCA Protein Assay Kit (cat. #23225)	Was used for quantification of total protein
PageRuler Prestained Protein Ladder (cat. #26616)	Was used for visualizing protein molecular weights during Western blotting
Primary antibodies	Rabbit polyclonal Anti-SNX3 antibody (cat. #ab56078), Rabbit polyclonal Anti-Transferrin Receptor antibody (cat. #ab193188), Mouse monoclonal Anti-beta Actin antibody [AC-15] (cat. #ab6276),

	Antibodies were diluted in 3% BSA in 1X TBST or 1X PBST for Western blotting or in 1% BSA, 0.05% Triton X-100 in PBS for immunofluorescence staining
Secondary antibodies	Goat Anti-Rabbit IgG H&L (HRP) (cat. #ab6721), Goat Anti-Mouse IgG H&L (HRP) (cat. #ab6789), Goat Anti-Rabbit IgG (H+L) Highly Cross-Adsorbed Secondary Antibody, Alexa Fluor™ Plus 647 (cat. #A32733) Antibodies were diluted in 3% BSA in 1X TBST or 1X PBST for Western blotting or in 1% BSA, 0.05% Triton X-100 in PBS for immunofluorescence staining
Clarity Western ECL Substrate (cat. #1705060)	Was used to visualize protein labeled with HRP-conjugated secondary antibodies
Erastin	Erastin (1 mg) (cat. #ab209693) was diluted in 1 mL DMSO and filtered with a 0.22 uM filter to yield a stock solution with a final concentration of 1.828 mM. The stock solution was aliquoted and stored at -20°C.
Ferrostatin-1	5 mg Ferrostatin-1 (cat. #SML0583-5MG) was diluted in DMSO to yield a stock solution with a final concentration of 10 mg/ml. The stock solution was aliquoted and stored at -20°C.
Deferoxamine mesylate (DFO)	5 mg of DFO (cat. #ab120727) was diluted in deionized water to yield a stock solution with a final concentration of 10 mg/ml. The stock solution was aliquoted and stored at -20°C.
BODIPY 581/591 C11	BODIPY 581/591 C11 Lipid Peroxidation Sensor (cat. #D3861) was aliquoted and diluted to a final concentration of 15 mM. The solution was stored at -20°C in the dark.
MitoSOX	50 ug of MitoSOX Mitochondrial Superoxide Indicator (cat. #M36008) was dissolved in 13 uL of deionized water to yield a stock solution with the final concentration of 5 mM. The solution was aliquoted and stored at -20°C in the dark.
Alamar blue	alamarBlue Cell Viability Reagent (cat. #DAL1025)
Perforation buffer	0.5% Triton X-100 in 1X PBS

Blocking buffer for immunofluorescence staining	1% BSA, 0.2% Triton X-100 in PBS
Antibody dilution buffer for immunofluorescence staining	1% BSA, 0.05% Triton X-100
Mounting medium containing DAPI	ProLong Diamond Antifade Mountant with DAPI (cat. #P36971)
PureZOL RNA Isolation Reagent (cat. #7326890)	Was used to isolate total RNA for RT-qPCR
LunaScript RT SuperMix Kit (cat. #NEB #E3010)	Was used to synthesize cDNA from total RNA
SYBR Green PCR Master Mix (cat. #4309155)	Was used to perform qPCR
Agarose (cat. #A9539-10G)	Was used for agarose gel electrophoresis
DirectLoad 1 kb DNA Ladder (cat. #D3937-1VL)	Was used for agarose gel electrophoresis
DreamTaq Green PCR Master Mix (2X) (cat. # K1081)	Was used for genomic PCR
SNX3 Human Gene Knockout Kit (CRISPR)	SNX3 - KN2.0, Human gene knockout kit via CRISPR, non-homology mediated (cat. #KN402354)
TransFectin Lipid Reagent (cat. #1703351)	Transfection reagent used for knockout and overexpression of SNX3
Opti-MEM Reduced Serum Medium (cat. #31985070)	Used for diluting plasmid DNA and TransFectin during transfection
Puromycin dihydrochloride (cat. #ab141453)	Was used as a selection agent for cells transfected with the CRISPR kit
LB agar, Miller (L3027-250G)	Was used for solid bacterial cultures

LB broth, Miller (cat. #L3152-1KG)	Was used for liquid bacterial cultures
SNX3-pEGFP plasmid	Provided by the lab (ligated in house)

Table 2. List of cell lines used

Abbreviation	**Description**
MDA-MB-231	Human breast adenocarcinoma
MDA-MB-436	Human breast adenocarcinoma
MDA-MB-468	Human breast adenocarcinoma
MCF-7	Human breast adenocarcinoma
HeLa	Human cervical adenocarcinoma

Cell culture

Cells were cultured at 37°C, 5% CO_2 in Dulbecco's Modified Eagle Medium (DMEM) supplemented with 10% fetal bovine serum (FBS), 1% Penicillin-Streptomycin, and 1% non-essential amino acids.

Cell passaging

At around 70% confluency the culture medium was aspirated, and the cells were washed twice with pre-warmed 1X PBS and incubated in Trypsin-EDTA 0.25% for 3 minutes at 37°C, 5% CO_2. Trypsin was neutralized with pre-warmed serum-containing DMEM. The cell suspension was collected into a 15 mL Falcon tube and centrifuged at 1000 g for 5 min at room temperature. The trypsin-containing medium was aspirated and the cell pellet was resuspended in 10 mL 1X PBS for counting. The PBS was removed by centrifugation at 1000 g for 5 min at room temperature. After counting, the cells were resuspended in the appropriate amount of complete culture medium, seeded to a fresh culture dish, and incubated at 37°C, 5% CO_2.

Erastin and ferrostatin-1 treatment

Aliquoted stock solutions were further diluted to a lower concentration in DMSO before treatment. Before treatment, cells were washed twice with 1X PBS, and the medium was replaced with a fresh complete culture medium. Erastin treatment was applied at around 70% confluency, or at least 24 hrs post-transfection. Ferrostatin-1 was added 1 hour prior to erastin treatment. Cells were incubated at 37°C, 5% CO_2.

Cell viability assay

The cell viability was measured with alamarBlue Cell viability reagent. 10,000 MDA-MB-231 cells were seeded onto each well of a 96-well plate in 200 uL of complete culture medium and incubated at 37°C, 5% CO_2. Erastin treatment was applied the following day, and cells were incubated 37°C, 5% CO_2. After 12 h of incubation, 20 uL of alamarBlue cell viability reagent were added to each well. The cells were incubated for an additional 4 hours in the dark at 37°C, 5% CO_2. The absorbance readings were taken at 570 nm and 600 nm using the iMark Microplate Absorbance Reader.

Flow cytometry

150,000 cells/well were seeded to a 6-well plate and incubated at 37°C 5% CO_2. The following day or upon reaching 70% confluency, the cells were treated with appropriate concentrations of erastin with or without Fer-1 pre-treatment, and incubated for 24 h at 37°C 5% CO_2. The cells were then stained with 1.5 mM BODIPY C11, according to the protocol by Martinez et al. (2020). Additionally, the cells were stained with SYTOX Blue according to the reagent manual. Flow cytometry analysis was performed using an Attune NxT Flow Cytometer. The results were analyzed using the FCS Express program.

SNX3 overexpression

One day before transfection, 150,000 cells (MDA-MB-231) were seeded on a 6-well plate in 2 mL of an antibiotic-free culture medium and incubated at 37°C, 5% CO2. 6 uL of TransFectin lipid reagent was diluted in 250 uL Opti-MEM or serum-free DMEM per each well. Similarly, 1 ug of plasmid DNA was diluted in 250 uL Opti-MEM or serum-free DMEM per well. The diluted TransFectin and plasmid were mixed and incubated at room temperature for 20 min. The mixture was then added directly to

cells in a serum-containing culture medium. Cells were incubated at 37°C, 5% CO2 for 4 hours or overnight, after which the transfection medium was replaced with a fresh complete culture medium.

SNX3 knockout

Cells were simultaneously transfected with 1 ug of pCas-Guide plasmid and 1 ug of linear donor using the same transfection protocol. The cells were passaged 48 hours post-transfection. After an additional 24 hours, the cells were treated with puromycin. Cells were allowed to grow for an additional 10 days, before further passaging.

Quantitative reverse transcription PCR

Total RNA was extracted from MDA-MB-231, MDA-MB-436, MDA-MB-468, MCF-7, and HeLa cells using PureZOL RNA Isolation Reagent according to the reagent manual. The purity of the RNA was assessed using Nanodrop 2000. The cDNA was produced from the RNA using LunaScript RT SuperMix Kit, according to the reagent manual. The qPCR reaction was performed using the SYBR Green PCR Master Mix, according to the reagent manual. The expression of SNX3 in different cell lines was normalized against GAPDH. Analysis of the expression data was performed using Microsoft Excel and GraphPad Prism 8.0.

Western blot

To isolate total protein, cells were lysed by adding 1X RIPA buffer containing 1X Halt Protease and Phosphatase inhibitors for 30 minutes on ice. The lysate was centrifuged at 15,000 rpm for 10 minutes, and the supernatant was collected. The total protein concentration of the samples was measured using the Pierce BCA Protein Assay Kit according to the manual. The samples were boiled with 1X Laemmli buffer at 95°C for 5 min prior to loading. 10 ug of the total protein was loaded into each well. The gels were run at 120V for 1-1.5 hours. Proteins from the gel were transferred to a PVDF membrane at 18V overnight in the transfer buffer. The membrane was blocked with 3% BSA in TBST for 1 hour, followed by three washing steps with TBST. The membrane was incubated with primary antibodies diluted in the blocking buffer for 1 hour at room temperature, followed by three washing steps with TBST. The membrane was incubated with secondary HRP-conjugated antibodies diluted in the blocking buffer for 1 hour at room

temperature, followed by three washing steps with TBST. The proteins were visualized using Clarity Western ECL Substrate and ChemiDoc MP imaging system.

Immunofluorescence staining

10,000 MDA-MB-231 cells were seeded per each well of an ibidi µ-Slide 8 Well chamber slide with ibiTreat coating. The following day, upon proper adhesion, the cells were incubated with 4% PFA for 10 min for fixation, washed, and incubated with the perforation buffer for 10 min, followed by washing with PBST. The cells were incubated with the blocking buffer for 30 min, followed by overnight incubation at +4°C with diluted primary antibodies. Cells were washed again, and incubated with the diluted secondary antibody for 2 hours in the dark at room temperature. Cells were washed again, and one drop of ProLong Diamond Antifade Mountant with DAPI was added to each well. The cells were imaged with Zeiss LSM 780 Confocal Microscope and EVOS M7000 imaging system. The images were analyzed using ImageJ.

Live cell staining

10,000 MDA-MB-231 cells were seeded per each well of an ibidi µ-Slide 8 Well chamber slide with ibiTreat coating. Upon reaching 70% confluency, cells were treated with 10 uM erastin and incubated at 37°C, 5% CO_2 for 6 hours. 1 mL of 0.5uM MitoSOX was then added to the cell medium. DAPI was added to stain the nuclei. The cells were imaged with the EVOS M7000 imaging system.

Genomic PCR

Total genomic DNA was extracted from cells at around 90% confluency using the PureLink Genomic DNA Mini Kit according to the manual. Primers were diluted in nuclease-free water to a concentration of 10 mM. Each PCR reaction tube contained 12.5 uL of DreamTaq Green PCR Master Mix (2X), 1.25 uL of diluted forward primer (final concentration of 0.5 mM), 1.25 uL of diluted reverse primer, and 300 ng of genomic DNA. The mixture was made up to a total volume of 25 uL with PCR-grade water. The following cycle parameters were used:

Table 3. PCR cycle parameters

Temperature	**Time**	
95°C	3 min	
95°C	30 s	45x
50°C or 52°C	30 s	
72°C	1 min	
72°C	20 min	
4°C	Infinite hold	

Data collection and statistical analysis

Data from the cell viability assay and qPCR was collected and analyzed using Microsoft Excel. Statistical analyses for normality and significance, as well as visualization, were done in GraphPad Prism 8.

Results

Choice of cell line

To determine the appropriate cell line for experiments, expression of SNX3 in MDA-MB-231, MDA-MB-436, MDA-MB-468, and MCF-7 triple-negative breast cancer cell lines was assessed with qPCR. Unfortunately, no non-cancerous breast tissue cell lines were available, so HeLa was used as a baseline control. qPCR results revealed that the expression of SNX3 was significantly increased in MDA-MB-436, MDA-MB-468, and MCF-7 cells compared with HeLa (see Fig. 7A). There was no significant difference in the level of SNX3 between MDA-MB-231 cells and HeLa. The result is consistent with the RNA-seq expression data from the Expression Atlas and The Human Protein Atlas databases (see Fig. 7B and C respectively) (Karlsson et al., 2021; Moreno et al., 2022).

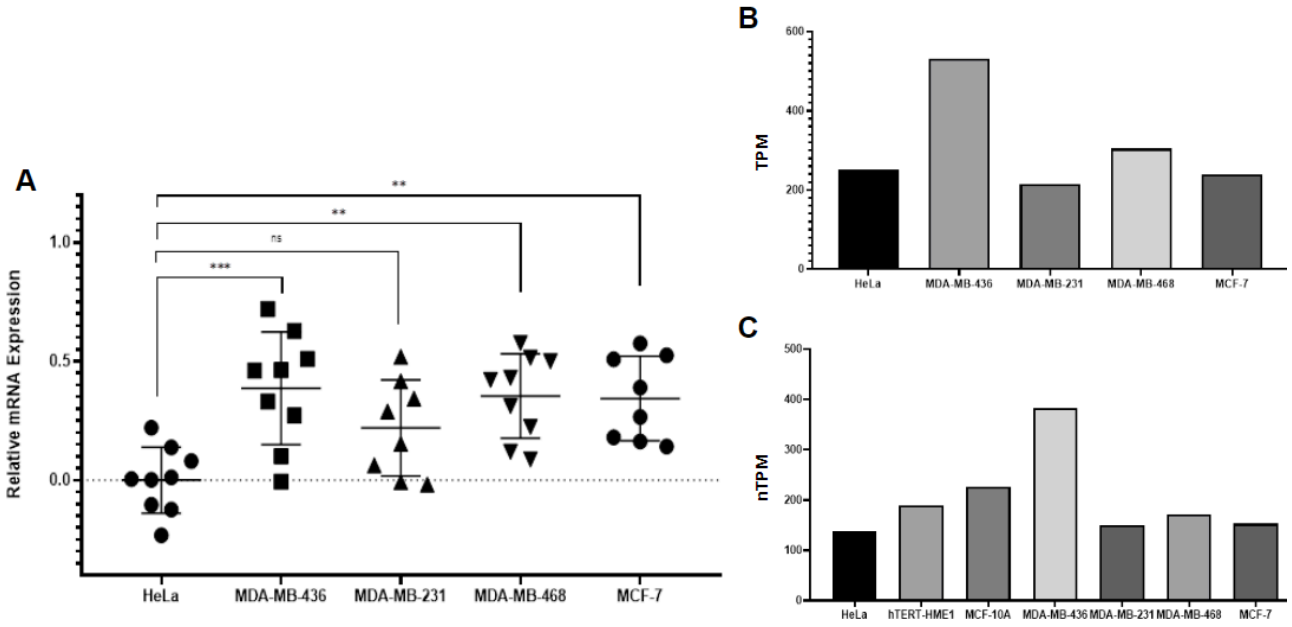

Figure 7. Relative expression of SNX3 in different cell lines. **A.** Log transformed values of $2^{-\Delta\Delta Ct}$ for SNX3 obtained from qPCR. The expression was normalized to GAPDH. The statistical significance was determined using ordinary one-way ANOVA (P=0.0006). The normality of the data was assessed using Shapiro-Wilk and Kolmogorov-Smirnov tests. The significance between different samples was assessed using Tukey's multiple comparisons test. **B.** Expression data obtained from the Expression Atlas database. TPM - transcripts per million. **C.** Expression data obtained from The Human Protein Atlas database. hTERT-HME1 and MCF-10A are non-cancerous immortalized cell lines obtained from the mammary gland tissue (Karlsson et al., 2021). nTPM - normalized TPM.

Based on the moderate level of SNX3 expression, suitable for overexpression and knockout, as well as the fact that this cell line has been extensively used in SNX3-related research, the MDA-MB-231 cell line was chosen for further experiments (Cicek et al., 2022; Öyken, 2020).

Effective concentrations of erastin and ferrostatin-1

To induce ferroptosis in the MDA-MB-231 cells, erastin was used. Erastin is a small-molecule compound which disrupts the import of cystine by system Xc^- (Dixon et al., 2012). Therefore, erastin treatment leads to the depletion of GSH and impairs the activity of the GPX4-mediated antioxidant defence. This makes cells susceptible to the buildup of lipid hydroperoxides and subsequent ferroptotic cell death.

To establish the effective concentration of erastin for treatment experiments, MDA-MB-231 cells were incubated for 24 hours with different concentrations of erastin (2.5 uM, 5 uM, 10 uM, and 15 uM). Since ferroptosis has a negative effect on cell viability, the effect of erastin was assessed with the Alamar Blue cell viability assay (H. Wang et al., 2022). DMSO was used as a solvent control. It was determined that there was no significant difference between 2.5 uM and 5 uM concentrations of erastin and DMSO (see Fig. 8). On the other hand, treatment with 10 uM and 15 uM erastin significantly decreased cell viability in relation to DMSO. Based on this result, 10 uM erastin was chosen for further treatment experiments.

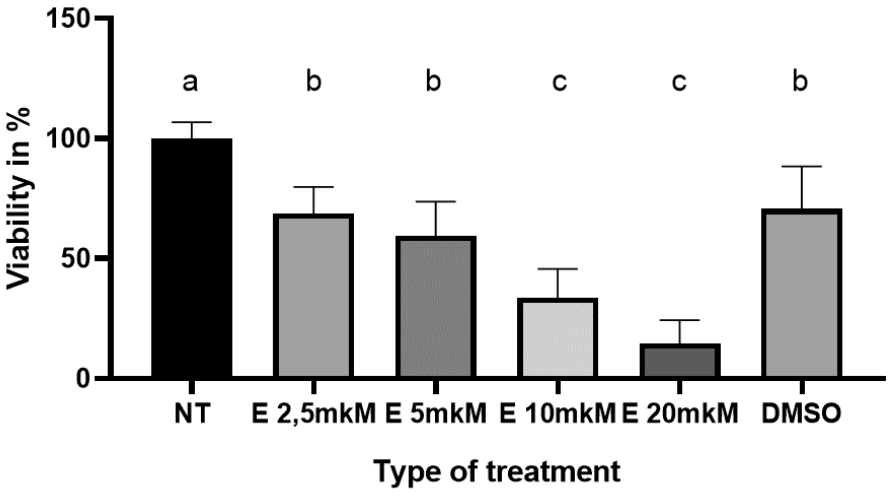

Figure 8. Effect of erastin treatment on viability in MDA-MB-231 cells after 24 h incubation. The cell viability was assessed using the Alamar blue reagent. DMSO was used as a solvent

control. NT - no treatment. Letters “a”, “b”, and “c” indicate statistically significant differences between treatment groups. There is no significant difference between groups labelled with the same letters. The statistical significance was determined using ordinary one-way ANOVA ($P<0.0001$). The normality of the data was assessed using the Shapiro-Wilk test. The significance between different samples was assessed using Tukey's multiple comparisons test.

Ferrostatin-1 prevents morphological changes induced by erastin treatment

Ferrostatin-1 (Fer-1) is a highly effective inhibitor of ferroptosis (Skouta et al., 2014). It is a synthetic antioxidant capable of scavenging lipid ROS and decreasing levels of intracellular ferrous iron. Therefore, ferrostatin acts downstream of erastin and is expected to prevent erastin-induced ferroptosis (see Fig. 9) . In our experiments, we planned to use Fer-1 to counteract the effects of erastin, and eventually map where SNX3 may act in the ferroptosis pathway.

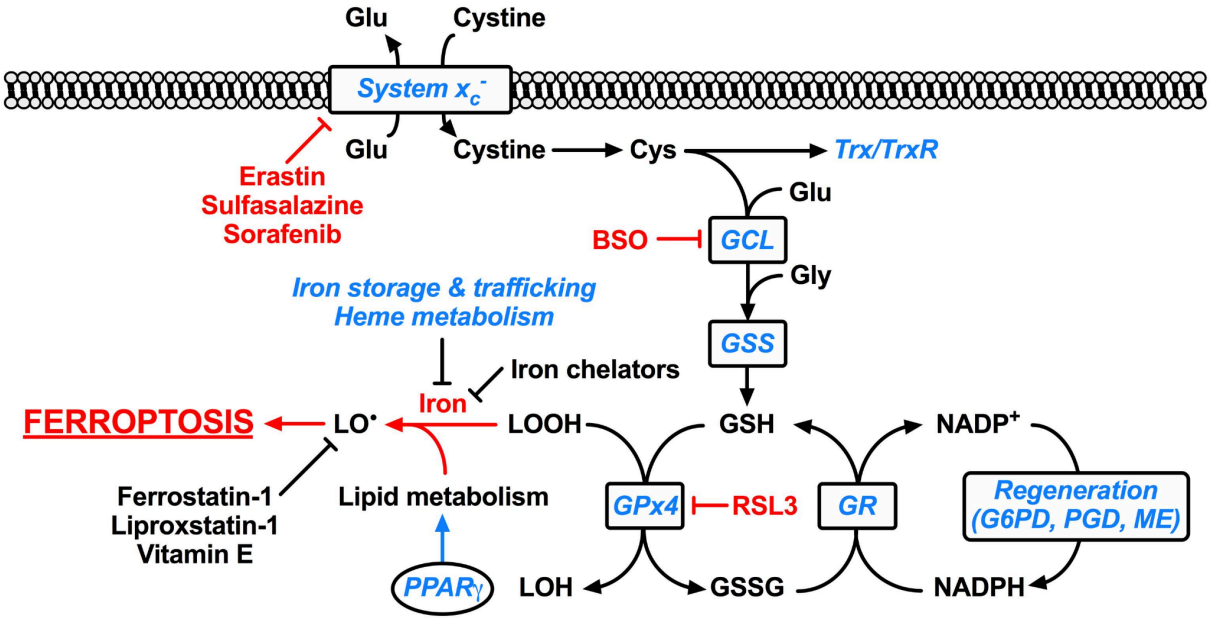

Figure 9. Ferroptosis regulation pathway. Ferrostatin exerts its anti-ferroptotic effects downstream of erastin (adapted from Abdalkader et al., 2018).

MDA-MB-231 cells were treated with varying concentrations of erastin (2.5 uM, 5 uM, 10 uM, and 15 uM) and incubated for 24 hours. Fer-1 (2.5 uM or 5 uM) was added 1 h prior to erastin treatment. DMSO treatment was used as a solvent control. Microscopic observation revealed that erastin-only treatment leads to significant changes in morphology, causing increased granularity, irregular shape, and cell

detachment in a concentration-dependent manner (see Fig 10 and Appendix fig. 9). These effects were partially or completely prevented in cells pre-treated with Fer-1, with higher efficiency at 5uM concentration. Based on these results, 5 uM Fer-1 was chosen for further experiments.

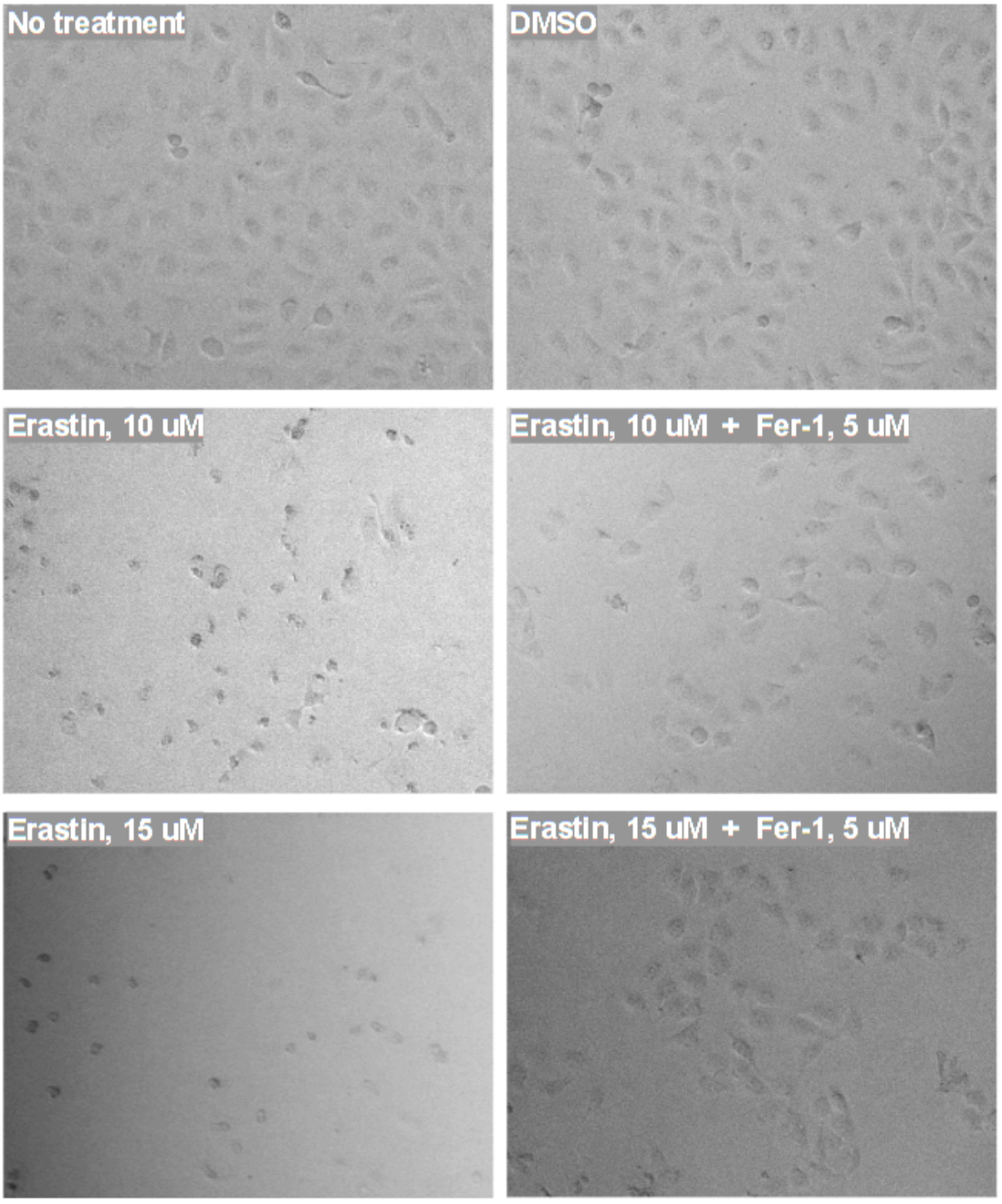

Figure 10. Effects of erastin treatment on the morphology of MDA-MB-231 cells are prevented by Fer-1 pre-treatment. DMSO was used as a solvent control.

Erastin treatment induces lipid peroxidation in MDA-MB-231 cells

To confirm that the effects of erastin treatment on MDA-MB-231 cells are indeed associated with ferroptosis, the cells were further analyzed for levels of lipid peroxidation. Accumulation of toxic lipid peroxides in the cellular membranes is one of the main hallmarks of ferroptosis (Stockwell, 2022). This process was visualized using the BODIPY 581/591 C11 fluorescent lipid peroxidation sensor. The dye contains a polyunsaturated hydrocarbon part and localizes to the membranes of live cells (Martinez et al., 2020). In the event of ferroptosis, the probe becomes oxidized and shifts its fluorescence from red (581/591 nm) to green (488/510 nm). Unfortunately, at the time I was not aware that BODIPY C11 would produce green fluorescence in cells undergoing ferroptosis, and the fluorescence was imaged in the red spectrum.

MDA-MB-231 cells were stained with 1.5 uM C11 BODIPY 12 hours after 10 uM erastin treatment. Live imaging revealed that erastin treatment resulted in reduced fluorescence emitted by the BODIPY C11 probe, suggesting that the probe was oxidized due to the accumulation of lipid peroxides. Additionally, treated cells have significant changes in morphology, compared with the untreated cells.

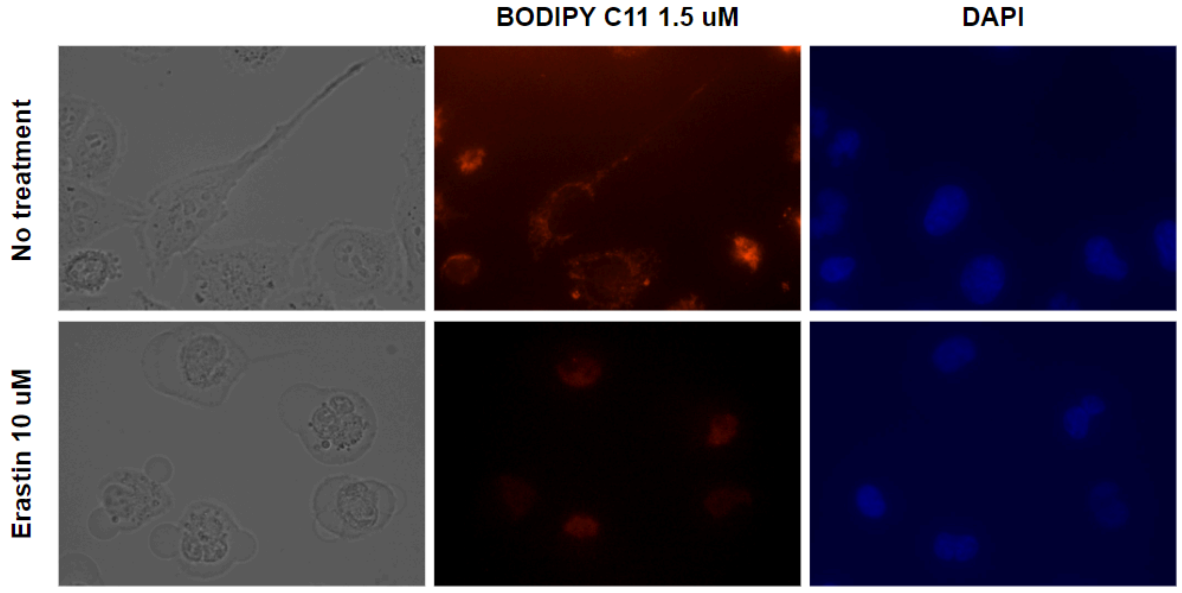

Figure 11. Live fluorescence staining images of untreated and 10 uL erastin-treated MDA-MB-231 cells. Left - bright field image. Middle - BODIPY C11 fluorescence. Right - DAPI fluorescence.

Ferrostatin-1 prevents lipid peroxidation induced by erastin treatment

MDA-MB-231 cells were treated with varying concentrations of erastin (2.5 uM, 5 uM, 10 uM, and 15 uM) 24 hours prior to staining. 5 uM Fer-1 was added 1 h before erastin treatment. DMSO was used as a solvent control. The cells were stained with BODIPY 581/591 C11 to assess the extent of lipid peroxidation and SYTOX Blue dead cell stain to assess the effect on cell viability. Similarly to the previous experiment, the reduction in the red signal was used as an indicator of ferroptosis. Measurements were taken on the Attune NxT flow cytometer using the 585/16 nm YL-1 filter for BODIPY C11 and 450/40 nm VL-1 filter for SYTOX Blue.

The analysis revealed that erastin treatment notably decreased cell viability and increased the amount of lipid peroxidation, as shown by the increase of the SYTOX Blue signal and the decrease of the BODIPY C11 signal (see Fig. 12 and Appendix fig. 12). The effect was completely reversed in cells pre-treated with 5 uM Fer-1, and the resulting plots resemble the results of DMSO treatment. It is therefore likely that treatment with erastin specifically induces ferroptosis in MDA-MB-231 cells.

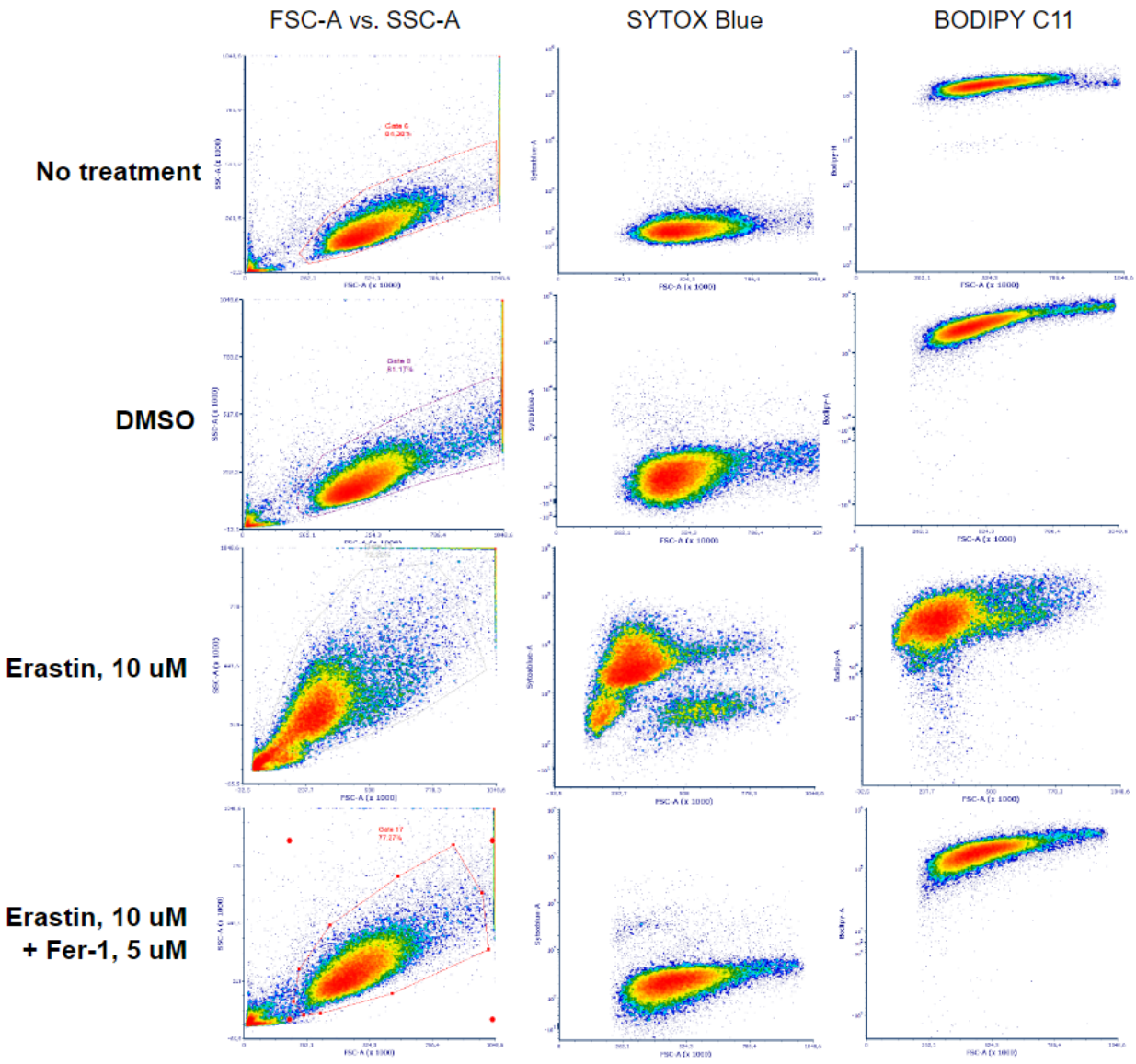

Figure 12. Flow cytometry density plots demonstrating the effects of 10 uM erastin treatment with and without 5 uM Fer-1 pre-treatment. DMSO was used as a solvent control. Higher values of the SYTOX Blue signal indicate decreased viability and increased cell death. Lower values of the BODIPY C11 indicate an increased level of lipid peroxidation. The signal was gated on the FSC-A vs. SSC-A plot around the major cell cluster to exclude cell debris. FSC-A - area of the forward scatter signal. SSC-A - area of the side scatter signal. The data was analyzed and plotted using the FCS Express software.

Erastin treatment leads to the accumulation of mitochondrial superoxide

Another hallmark of ferroptosis is deregulated mitochondrial metabolism. It has been reported that cells undergoing ferroptosis have irregularly shaped and sized mitochondria, in some cases enlarged, in others, shrunken (Stockwell, 2022). One of the markers of ferroptosis in mitochondria is the accumulation of mitochondrial superoxide (G.-H. Chen et al., 2022; Lyamzaev et al., 2023). To further confirm that erastin treatment of MDA-MB-231 cells specifically induces ferroptosis, cells were stained with 2.5 uM MitoSOX Red mitochondrial superoxide stain, 12 hours after 10 uM erastin treatment. Oxidation of the MitoSOX reagent by mitochondrial superoxides produces bright red fluorescence.

Live imaging has revealed some changes in the nuclear and cellular morphology and the accumulation of superoxides in the mitochondria of erastin-treated cells, as indicated by red fluorescence (see Fig. 13). The effects were not observed in untreated cells. Notably, no DNA fragmentation was observed, which is common for other cell death modalities. The results provide further evidence that erastin treatment in MDA-MB-231 cells specifically induces ferroptosis.

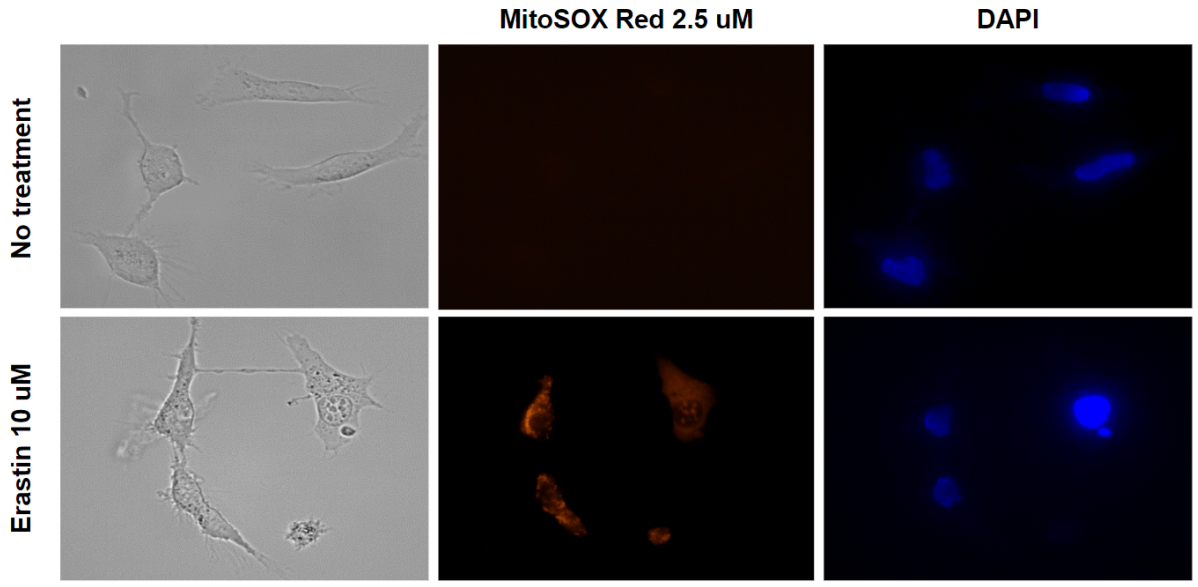

Figure 13. Live fluorescence staining images of untreated and 10 uL erastin-treated MDA-MB-231 cells. Left - bright field image. Middle - MitoSOX Red fluorescence. Right - DAPI fluorescence.

Overexpression of SNX3 with a SNX3-containing plasmid was unsuccessful

To investigate the relationship between SNX3 and ferroptosis, it was important to produce MDA-MB-231 cells with varying levels of SNX3 expression. To achieve SNX3 overexpression, we decided to conduct transient transfection of the cells with an SNX3-pEGFP-containing plasmid (see Appendix fig. 13). The plasmid was transfected using the TransFectin lipid reagent according to the reagent manual. Transfection efficiency of around 40-50% was achieved the next day (see Fig 14A). Despite the relatively high efficiency of transfection, most of the transfected cells would start exhibiting abnormal round morphology and detach by 48 h post-transfection (see Fig. 14B).

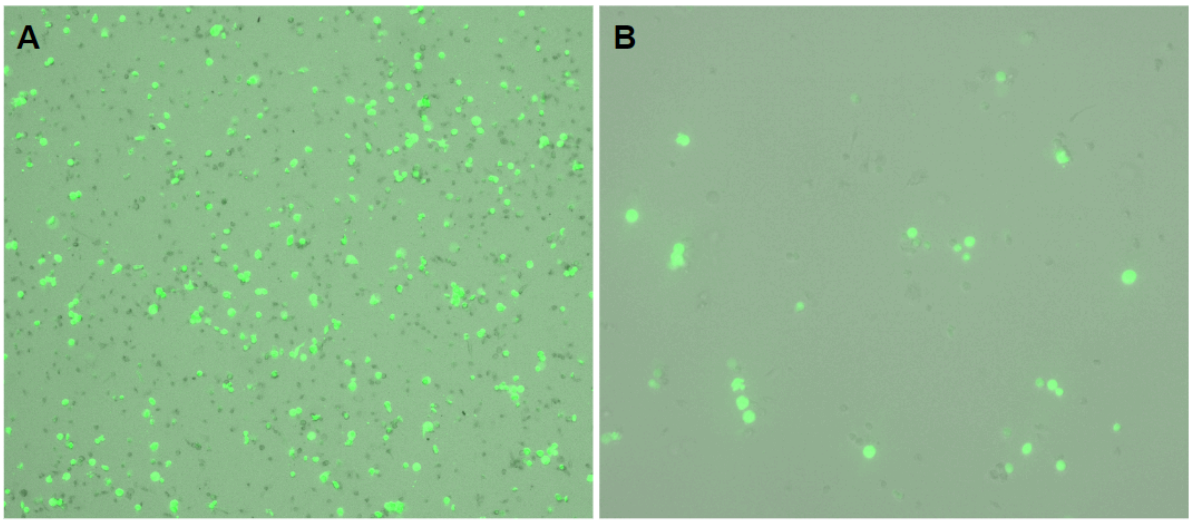

Figure 14. MDA-MB-231 cells after transfection with an SNX3-pEGFP plasmid. **A.** Around 40-50% of the cells 24 h post-transfection expressed GFP. **B.** By 48 h post-transfection, GFP-expressing cells started exhibiting round morphology, detaching, and dying.

To try to overcome the issue, a number of solutions have been tried one by one, ranging from changing the incubation conditions to altering the compositions of culture and transfection media (see Table 4). In 2015, Gao et al. reported that the presence of transferrin and glutamate in the medium was necessary and sufficient for the induction of ferroptosis. Since we were using a GlutaMAX culture medium, which was further supplemented with 1% non-essential amino acids; and since Opti-MEM contains transferrin, it was hypothesized that the abnormal cell death could be ferroptosis, caused by the dramatic increase in the level of SNX3.

Table 4. List of tested transfection conditions

Condition	Parameters
Incubation time in the transfection medium	Overnight, 12 hrs, 4hrs
Plasmid	SNX3-pEGFP, empty vector, from stock or newly isolated with Miniprep
Plasmid concentration	1 ug/mL, 0.5 ug/mL, 0.25 ug/mL, 0.1 ug/mL
TransFectin concentration	3 uL/mL, 1.5 uL/mL, 1 uL/mL, 0.5 uL/mL
Antibiotics in the medium	1% Pen/Strep or without antibiotic
Medium for the dilution of DNA and TransFectin	DMEM (without serum) or Opti-MEM
Transfection medium	DMEM (10% FBS) or Opti-MEM
Iron in the medium	Normal or chelated with Deferoxamine
Amino acid supplementation	With or without the addition of non-essential amino acids

To test the hypothesis, Opti-MEM was replaced with plain DMEM for plasmid and TransFectin dilution. Additionally, the iron in the medium was chelated prior to transfection with deferoxamine, a potent iron chelator known to inhibit ferroptosis. Unfortunately, none of the conditions tested yielded an improvement in cell survival or transfection efficiency. Therefore, no further experiments with SNX3 overexpression were conducted.

CRISPR-mediated knockout of SNX3 requires further verification

To see if the lack of SNX3 would affect the susceptibility or resistance to ferroptosis, the MDA-MB-231 cells were transfected with 1 ug of pCas-Guide vector and 1 ug of linear donor sequence from the OriGene KN2.0 non-homology mediated CRISPR knockout kit (see Fig. 15), using the same transfection protocol. Two transfections were made, one for each gRNA.

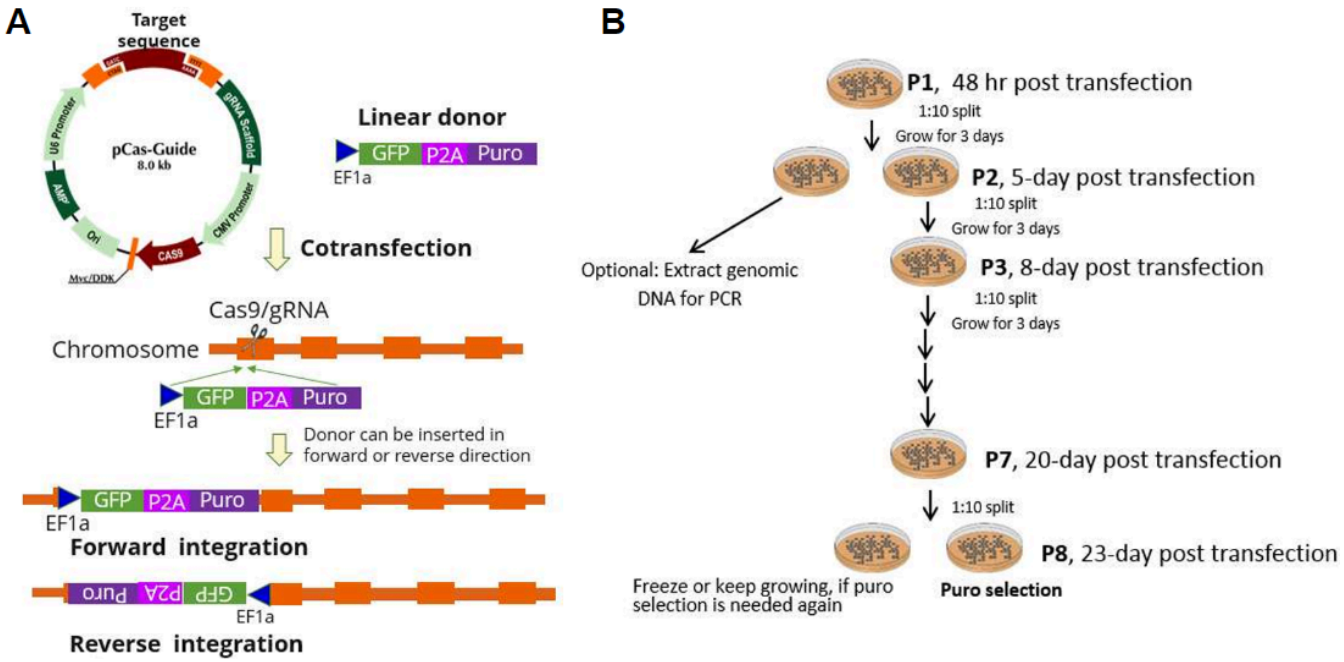

Figure 15. Diagram of the KN2.0 non-homology-mediated CRISPR knockout kit. **A.** The kit includes two pCas-Guide constructs, each with a different guide RNA sequence, and a linear donor. The linear donor contains genes for puromycin resistance and GFP. The linear donor can integrate into the site of Cas-generated cleavage in two directions. **B.** Cell passaging protocol after transfection suggested by the manufacturer.

The cells were split 48 post-transfection. Due to time restrictions, the selection with puromycin was started early, after the second split. The cells expressing GFP (see Fig. 16) were allowed to grow to around 80% confluency before further passages.

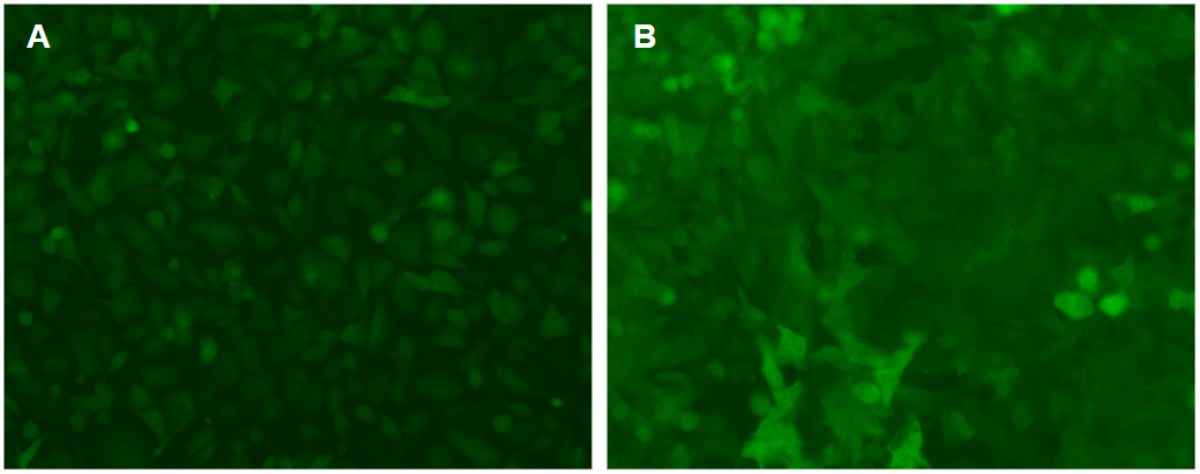

Figure 16. Green fluorescence image of transfected expression at >90% prior to total DNA isolation. **A.** Cells transfected with the gRNA1-containing construct. **B.** Cells transfected with the gRNA2-containing construct.

Since there was a possibility that the donor remained episomal, genomic PCR was conducted to screen for potential integration of the linearized cassette. Since the donor could be integrated in two directions, five pairs of primers were tested (see Fig. 17 A, C). A band of matching size was detected with the primer pair 5, indicating potential reverse integration of the linear donor in some of the gRNA1-transfected cells. However, the possibility of an incomplete (heterozygous) knockout cannot be excluded. The primer pair 1, which was expected to show a band in all samples, did not produce any product. This result was not affected by using different annealing temperatures, suggesting a fault in the primer design or manufacturing.

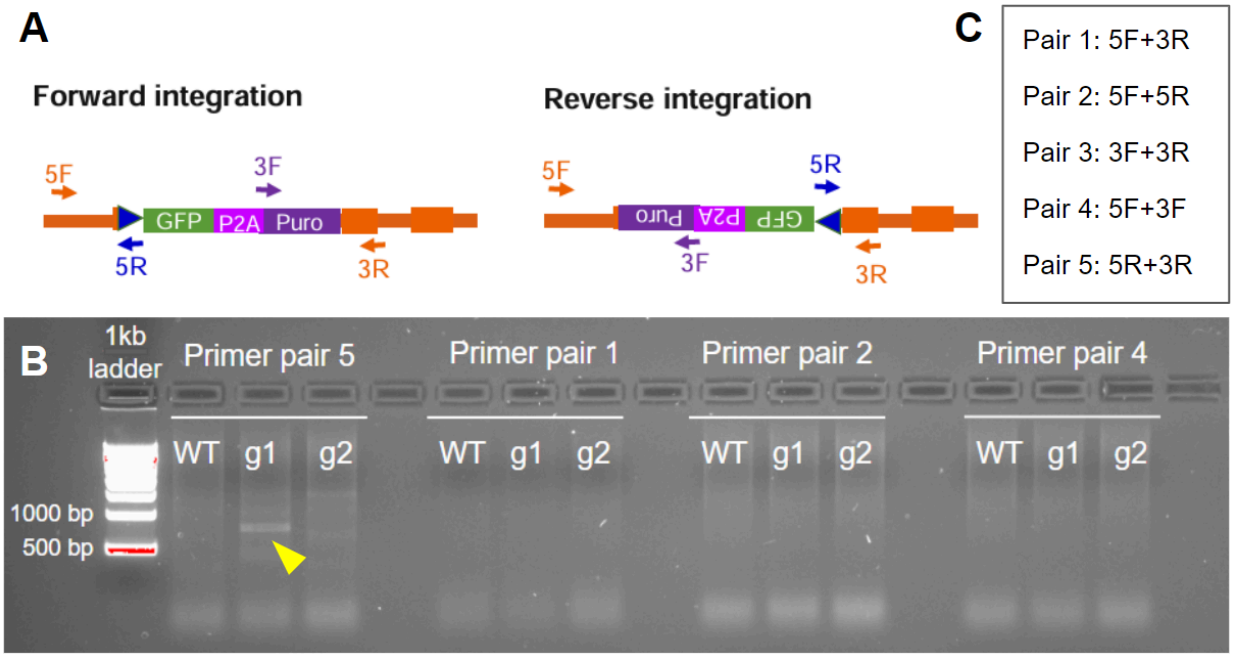

Figure 17. Setup and results of PCR. **A.** Scheme of primer locations used for PCR. **B.** Agarose gel electrophoresis of the resulting PCR product. The yellow arrow points at the band indicating potential reverse integration of the donor **C.** Combinations of primers used for PCR. The annealing temperature was set to 50°C.

Making any conclusive statements regarding the success of the knockout requires isolating and expanding single colonies with further confirmation of the biallelic knockout with PCR. To this end, a portion of the cells was seeded onto 96-well plates by serial dilution.

Immunofluorescence staining and Western blotting experiments were unsuccessful due to faulty antibodies

To assess the expression and localization of SNX3 and TFRC in the knockout cells, immunofluorescence staining experiments were conducted. Cells were fixed, permeabilized, incubated overnight with either anti-SNX3 or anti-TFRC (Abcam primary antibodies, and finally incubated for 2 hours with a secondary antibody conjugated to AlexaFluor 647. The nuclei were stained with a DAPI-containing mounting medium. The cells were imaged using a Zeiss laser scanning confocal microscope.

Interestingly, the obtained images show that SNX3 is uniformly dispersed throughout the cytoplasm of both the normal and gRNA-transfected cells (see Fig. 18). This is in contrast to the expected pattern of SNX3 staining, which is supposed to be localized to intracellular membranes (see Appendix fig. 14). Additionally, the red signal coming from the secondary antibody was detected in every cell present in the culture (see Appendix fig. 15).

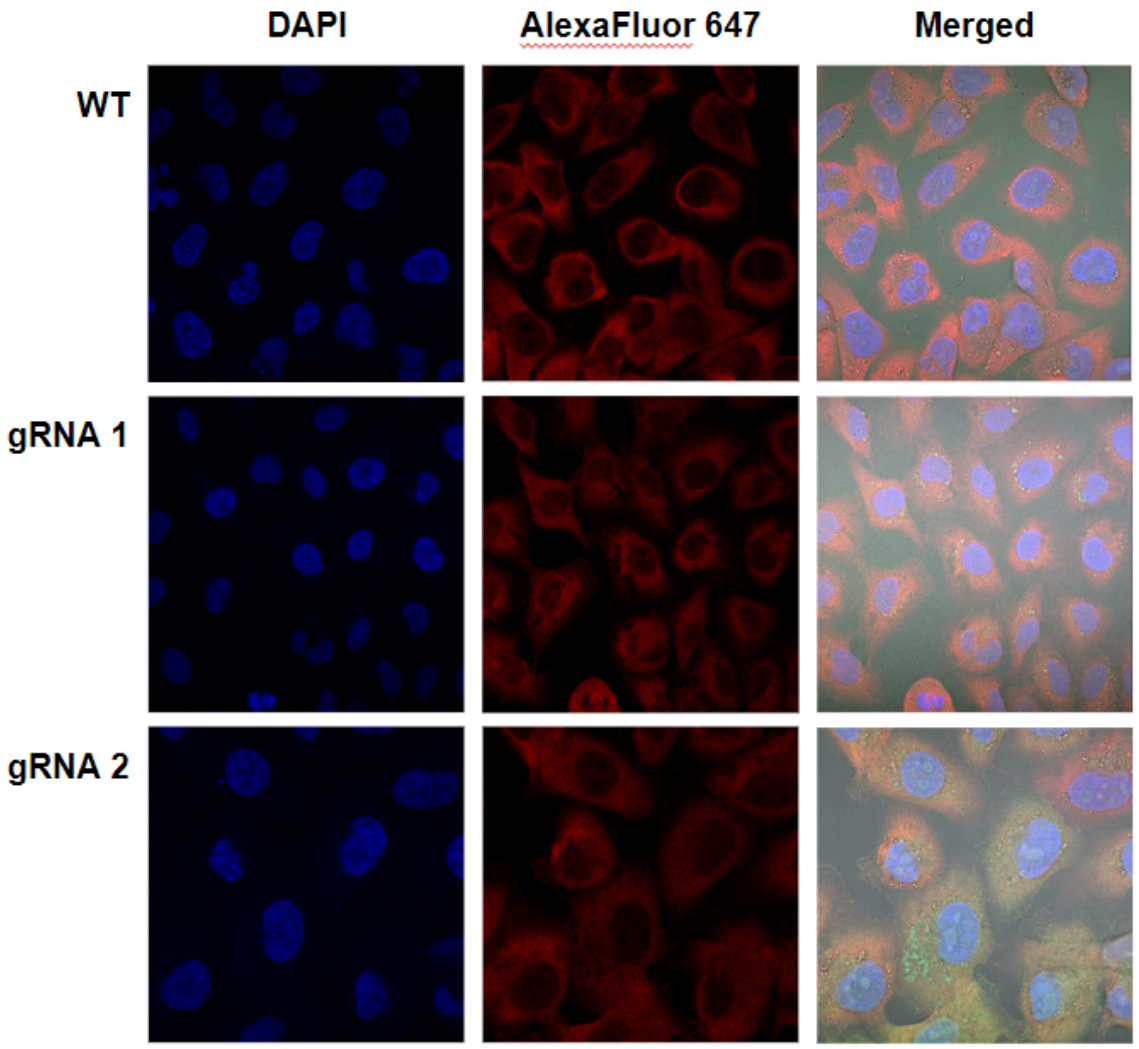

Figure 18. Immunofluorescence staining of SNX3 in normal and gRNA-transfected MDA-MB-231 cells. Nuclei were visualized with DAPI (blue). SNX3 was visualized with a secondary antibody conjugated to AlexaFluor 647 Plus (red).

On the other hand, images of TFRC show unexpected fluorescence inside the nucleus (see Fig 19). This was confirmed by taking z-stacks of the nuclear cross section (see Appendix fig. 16). This is also different from the images provided by the manufacturer (see Appendix fig. 17).

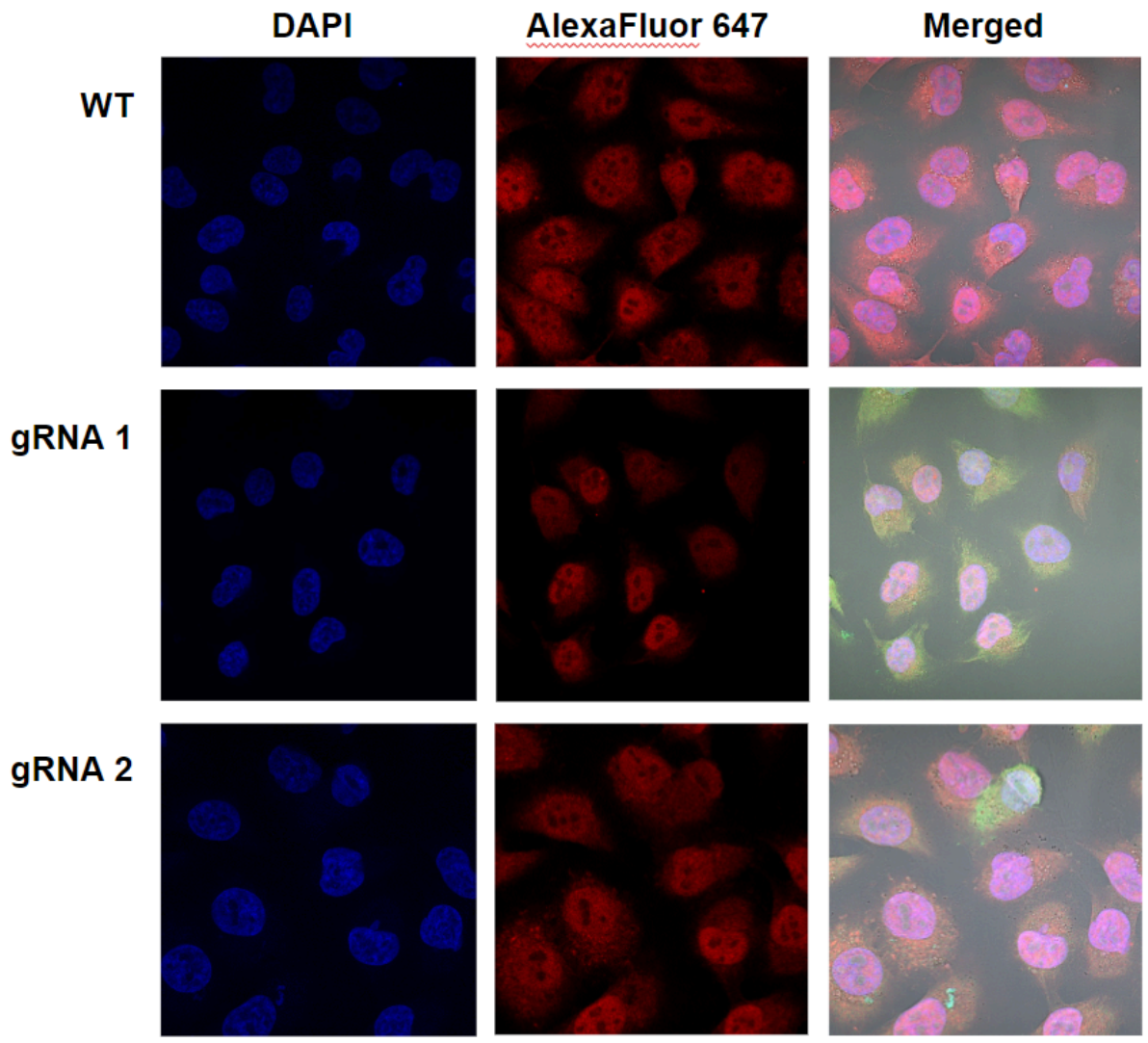

Figure 19. Immunofluorescence staining of TFRC in normal and gRNA-transfected MDA-MB-231 cells. Nuclei were visualized with DAPI (blue). TFRC was visualized with a secondary antibody conjugated to AlexaFluor 647 Plus (red).

Interestingly, prior Western blot analyses of SNX3 and TFRC expression in breast cancer cell lines consistently showed nonspecific binding, despite multiple attempts under different conditions (see Fig. 20). Additionally, the anti-SNX3 antibody (#ab56078) has been discontinued by the manufacturer and is no longer in sale. This led us to the conclusion that the issue was in the quality of the antibodies. Due to time restrictions, it was not possible to repeat the experiments with a different set of antibodies.

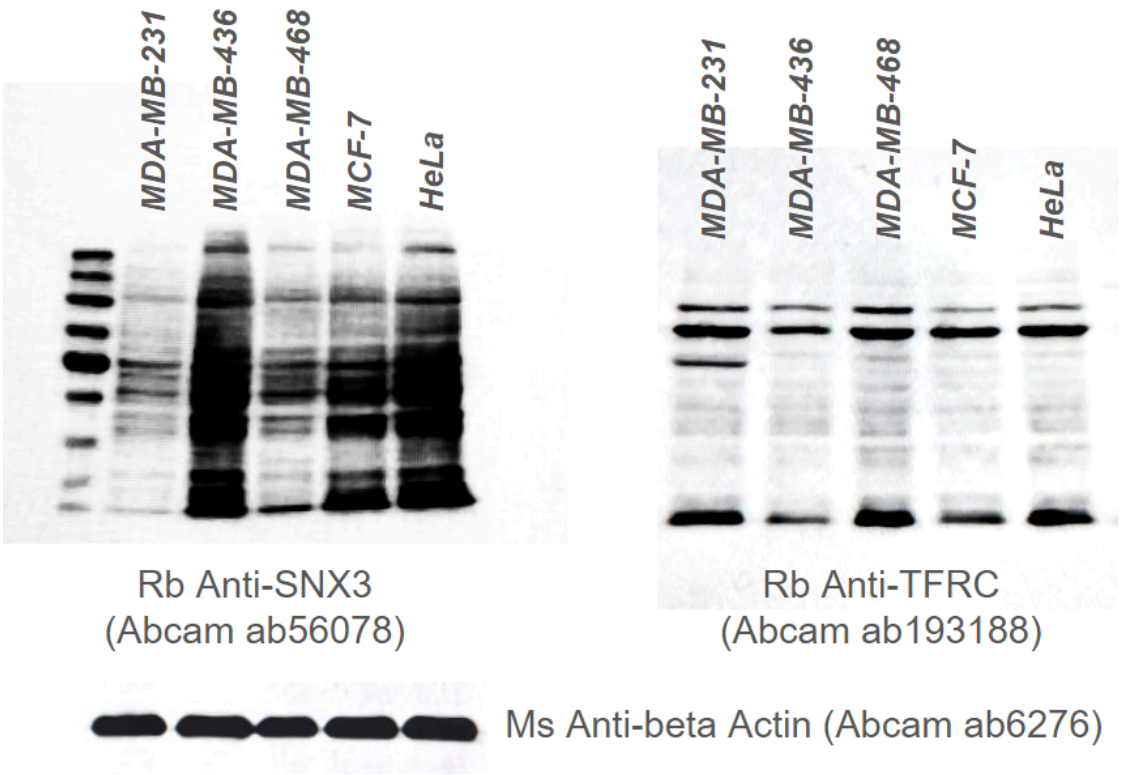

Figure 20. Nonspecific binding of the anti-SNX3 and anti-TFRC antibodies during Western blot. HRP-conjugated secondary antibodies were used. The proteins were visualized using the ECL substrate.

Discussion

During the course of the study, expression levels of SNX3 were compared between several breast cancer cell lines using RT-qPCR. According to the obtained data, there was a significantly higher expression of SNX3 in MDA-MB-436, MDA-MB-468, and MCF-7 cells compared to the baseline control (HeLa), but not in MDA-MB-231 cells. The result was consistent with data previously deposited to Expression Atlas and Human Cell Atlas databases. Due to its moderate levels of SNX3 expression and a history of being used for SNX3-related research, the MDA-MB-231 cell line was chosen for further experiments.

The optimal concentration of a ferroptosis-inducing molecule erastin was determined to be 10 uM using a cell viability assay. Interestingly, other studies identify the IC50 value of erastin to be as little as 2.2 uM or as large as 40 uM specifically for the MDA-MB-231 cells (M. Li et al., 2020; H. Wang et al., 2022). Notably, the 2.5 uM concentration of erastin was able to induce changes in morphology, decrease in cell viability, and accumulation of lipid ROS (see Appendix fig. 9 and 11).

Morphologically, treatment with erastin caused such changes as cell shrinkage, detachment, and increased granularity (see Fig. 9). The effect of erastin on cell morphology was also noticeable during flow cytometry, as the tight cluster of cells became more dispersed upon treatment, indicating increased granularity and changes in cell size (see Fig. 12 and Appendix fig. 11).

Erastin treatment was also shown to specifically induce ferroptosis, as indicated by the noticeable increase in lipid peroxidation, buildup of mitochondrial ROS, and lack of fragmentation of the cellular and nuclear membranes. Additionally, pre-treatment with 5 uM Fer-1 was shown to effectively inhibit the negative effects of erastin on cell morphology, viability, and ROS accumulation.

To investigate the hypothesis that SNX3 might be involved in ferroptosis via its role in the regulation of TFRC recycling, overexpression of SNX3 by transfection with the SNX3-pEGFP plasmid was attempted, albeit unsuccessfully. A large number of transfection conditions have been tested with no noticeable improvement. One of the possible explanations for such a result might be the toxicity of the plasmid itself.

As another way to test the relationship between SNX3 expression and susceptibility to ferroptosis, SNX3 was knocked out in MDA-MB-231 cells with a CRISPR kit. In this study, the knockout procedure was attempted quite late, so the time for the isolation and expansion of clones was insufficient. However, the results of the genomic PCR indicate potential knockout in at least some of the cells. Lastly, immunofluorescence staining and Western blotting experiments suggest that the antibodies against SNX3 and TFRC are unsuitable for future use.

Further research should involve the optimization of the transfection protocol for the overexpression of SNX3; confirmation of biallelic knockouts in isolated clones with PCR; and the comparison of SNX3 and TFRC expression levels in the obtained cells with RT-qPCR. The cells should subsequently be subjected to erastin treatment, and the response assessed with Alamar Blue, SYTOX Blue, and MitoSOX. The use of BODIPY C11 should be avoided in cells expressing GFP. Western blotting and immunofluorescence studies should be repeated with fresh antibodies to assess the effect of SNX3 overexpression and knockout on the levels of TFRC protein and its localization. Since SNX3 is responsible for the rescue of TFRC from early endosomes, it is possible that in SNX3-deficient cells, TFRC could be localized to late endosomes and lysosomes. As such, colocalization of TFRC with lysosomal markers like Lamp1 could be assessed. Additionally, other ferroptosis inducers and inhibitors acting at different steps of the ferroptosis pathway could be used to establish, whether SNX3 acts up or downstream of GPX4.

Conclusion

In the present study, it was hypothesized that sorting nexin 3, an adaptor of the retromer complex, could play a role in ferroptosis due to its involvement in the recycling of transferrin receptor 1, TFRC, an accurate marker of ferroptosis. Several objectives put forward at the beginning of the study have been accomplished. First, the effective concentration of erastin treatment in MDA-MB-231 cells was established to be 10 uM using the Alamar blue cell viability assay. Second, the effects of erastin on cellular morphology, viability and biochemical markers such as lipid ROS and mitochondrial ROS have been clearly demonstrated. Additionally, it was shown that pre-treatment with 5 uM Fer-1 was able to prevent all of those effects of erastin treatment, suggesting that erastin treatment specifically induces ferroptosis in MDA-MB-231 cells.

Reference list

Abdalkader, M., Lampinen, R., Kanninen, K. M., Malm, T. M., & Liddell, J. R. (2018). Targeting Nrf2 to Suppress Ferroptosis and Mitochondrial Dysfunction in Neurodegeneration. *Frontiers in Neuroscience*, *12*. https://doi.org/10.3389/fnins.2018.00466

Aisen, P. (2004). Transferrin receptor 1. *The International Journal of Biochemistry & Cell Biology*, *36*(11), 2137–2143. https://doi.org/10.1016/j.biocel.2004.02.007

Amaral, E. P., Costa, D. L., Namasivayam, S., Riteau, N., Kamenyeva, O., Mittereder, L., Mayer-Barber, K. D., Andrade, B. B., & Sher, A. (2019). A major role for ferroptosis in Mycobacterium tuberculosis–induced cell death and tissue necrosis. *Journal of Experimental Medicine*, *216*(3), 556–570. https://doi.org/10.1084/jem.20181776

Anderson, C. P., Shen, M., Eisenstein, R. S., & Leibold, E. A. (2012). Mammalian iron metabolism and its control by iron regulatory proteins. *Biochimica et Biophysica Acta (BBA) - Molecular Cell Research*, *1823*(9), 1468–1483. https://doi.org/10.1016/j.bbamcr.2012.05.010

Angelova, P. R., Choi, M. L., Berezhnov, A. V., Horrocks, M. H., Hughes, C. D., De, S., Rodrigues, M., Yapom, R., Little, D., Dolt, K. S., Kunath, T., Devine, M. J., Gissen, P., Shchepinov, M. S., Sylantyev, S., Pavlov, E. V., Klenerman, D., Abramov, A. Y., & Gandhi, S. (2020). Alpha synuclein aggregation drives ferroptosis: An interplay of iron, calcium and lipid peroxidation. *Cell Death & Differentiation*, *27*(10), Article 10. https://doi.org/10.1038/s41418-020-0542-z

Arosio, P., Ingrassia, R., & Cavadini, P. (2009). Ferritins: A family of molecules for iron storage, antioxidation and more. *Biochimica et Biophysica Acta (BBA) - General Subjects*, *1790*(7), 589–599. https://doi.org/10.1016/j.bbagen.2008.09.004

Banjac, A., Perisic, T., Sato, H., Seiler, A., Bannai, S., Weiss, N., Kölle, P., Tschoep, K., Issels, R. D., Daniel, P. T., Conrad, M., & Bornkamm, G. W. (2008). The cystine/cysteine cycle: A redox cycle regulating susceptibility versus resistance to cell death. *Oncogene*, *27*(11), Article 11.

https://doi.org/10.1038/sj.onc.1210796

Bao, W.-D., Pang, P., Zhou, X.-T., Hu, F., Xiong, W., Chen, K., Wang, J., Wang, F., Xie, D., Hu, Y.-Z., Han, Z.-T., Zhang, H.-H., Wang, W.-X., Nelson, P. T., Chen, J.-G., Lu, Y., Man, H.-Y., Liu, D., & Zhu, L.-Q. (2021). Loss of ferroportin induces memory impairment by promoting ferroptosis in Alzheimer's disease. *Cell Death & Differentiation*, *28*(5), Article 5. https://doi.org/10.1038/s41418-020-00685-9

Brigelius-Flohé, R., & Maiorino, M. (2013). Glutathione peroxidases. *Biochimica et Biophysica Acta (BBA) - General Subjects*, *1830*(5), 3289–3303. https://doi.org/10.1016/j.bbagen.2012.11.020

Chen, C., Garcia-Santos, D., Ishikawa, Y., Seguin, A., Li, L., Fegan, K. H., Hildick-Smith, G. J., Shah, D. I., Cooney, J. D., Chen, W., King, M. J., Yien, Y. Y., Schultz, I. J., Anderson, H., Dalton, A. J., Freedman, M. L., Kingsley, P. D., Palis, J., Hattangadi, S. M., … Paw, B. H. (2013). Snx3 Regulates Recycling of the Transferrin Receptor and Iron Assimilation. *Cell Metabolism*, *17*(3), 343–352. https://doi.org/10.1016/j.cmet.2013.01.013

Chen, D., Chu, B., Yang, X., Liu, Z., Jin, Y., Kon, N., Rabadan, R., Jiang, X., Stockwell, B. R., & Gu, W. (2021). iPLA2β-mediated lipid detoxification controls p53-driven ferroptosis independent of GPX4. *Nature Communications*, *12*(1), Article 1. https://doi.org/10.1038/s41467-021-23902-6

Chen, G.-H., Song, C.-C., Pantopoulos, K., Wei, X.-L., Zheng, H., & Luo, Z. (2022). Mitochondrial oxidative stress mediated Fe-induced ferroptosis via the NRF2-ARE pathway. *Free Radical Biology and Medicine*, *180*, 95–107. https://doi.org/10.1016/j.freeradbiomed.2022.01.012

Chen, L., Dar, N. J., Na, R., McLane, K. D., Yoo, K., Han, X., & Ran, Q. (2022). Enhanced defense against ferroptosis ameliorates cognitive impairment and reduces neurodegeneration in 5xFAD mice. *Free Radical Biology and Medicine*, *180*, 1–12. https://doi.org/10.1016/j.freeradbiomed.2022.01.002

Chen, M., Zhang, Y., Jiang, K., Wang, W., Feng, H., Zhen, R., Moo, C., Zhang, Z., Shi, J., & Chen, C. (2022). Grab regulates transferrin receptor recycling and

iron uptake in developing erythroblasts. *Blood*, *140*(10), 1145–1155. https://doi.org/10.1182/blood.2021015189

Chen, X., Kang, R., Kroemer, G., & Tang, D. (2021). Broadening horizons: The role of ferroptosis in cancer. *Nature Reviews Clinical Oncology*, *18*(5), Article 5. https://doi.org/10.1038/s41571-020-00462-0

Chen, X., Yu, C., Kang, R., & Tang, D. (2020). Iron Metabolism in Ferroptosis. *Frontiers in Cell and Developmental Biology*, *8*. https://www.frontiersin.org/articles/10.3389/fcell.2020.590226

Cheng, J., Fan, Y.-Q., Liu, B.-H., Zhou, H., Wang, J.-M., & Chen, Q.-X. (2020). ACSL4 suppresses glioma cells proliferation via activating ferroptosis. *Oncology Reports*, *43*(1), 147–158. https://doi.org/10.3892/or.2019.7419

Cicek, E., Circir, A., Oyken, M., Akbulut Caliskan, O., Dioken, D. N., Guntekin Ergun, S., Cetin-Atalay, R., Sapmaz, A., Ovaa, H., Sahin, O., & Erson-Bensan, A. E. (2022). EGF-SNX3-EGFR axis drives tumor progression and metastasis in triple-negative breast cancers. *Oncogene*, *41*(2), Article 2. https://doi.org/10.1038/s41388-021-02086-9

Cingöz, H. (2019). *Investigation of SNX3 in colon cancer* [Master Thesis, Middle East Technical University]. https://open.metu.edu.tr/handle/11511/27939

Cullen, P. J., & Steinberg, F. (2018). To degrade or not to degrade: Mechanisms and significance of endocytic recycling. *Nature Reviews Molecular Cell Biology*, *19*(11), Article 11. https://doi.org/10.1038/s41580-018-0053-7

Dixon, S. J., Lemberg, K. M., Lamprecht, M. R., Skouta, R., Zaitsev, E. M., Gleason, C. E., Patel, D. N., Bauer, A. J., Cantley, A. M., Yang, W. S., Morrison, B., & Stockwell, B. R. (2012). Ferroptosis: An Iron-Dependent Form of Nonapoptotic Cell Death. *Cell*, *149*(5), 1060–1072. https://doi.org/10.1016/j.cell.2012.03.042

Dixon, S. J., & Stockwell, B. R. (2014). The role of iron and reactive oxygen species in cell death. *Nature Chemical Biology*, *10*(1), Article 1. https://doi.org/10.1038/nchembio.1416

Dixon, S. J., Winter, G. E., Musavi, L. S., Lee, E. D., Snijder, B., Rebsamen, M.,

Superti-Furga, G., & Stockwell, B. R. (2015). Human Haploid Cell Genetics Reveals Roles for Lipid Metabolism Genes in Nonapoptotic Cell Death. *ACS Chemical Biology*, *10*(7), 1604–1609. https://doi.org/10.1021/acschembio.5b00245

Doll, S., Proneth, B., Tyurina, Y. Y., Panzilius, E., Kobayashi, S., Ingold, I., Irmler, M., Beckers, J., Aichler, M., Walch, A., Prokisch, H., Trümbach, D., Mao, G., Qu, F., Bayir, H., Füllekrug, J., Scheel, C. H., Wurst, W., Schick, J. A., … Conrad, M. (2017). ACSL4 dictates ferroptosis sensitivity by shaping cellular lipid composition. *Nature Chemical Biology*, *13*(1), Article 1. https://doi.org/10.1038/nchembio.2239

Drakesmith, H., Nemeth, E., & Ganz, T. (2015). Ironing out Ferroportin. *Cell Metabolism*, *22*(5), 777–787. https://doi.org/10.1016/j.cmet.2015.09.006

Fang, X., Wang, H., Han, D., Xie, E., Yang, X., Wei, J., Gu, S., Gao, F., Zhu, N., Yin, X., Cheng, Q., Zhang, P., Dai, W., Chen, J., Yang, F., Yang, H.-T., Linkermann, A., Gu, W., Min, J., & Wang, F. (2019). Ferroptosis as a target for protection against cardiomyopathy. *Proceedings of the National Academy of Sciences*, *116*(7), 2672–2680. https://doi.org/10.1073/pnas.1821022116

Feng, H., Schorpp, K., Jin, J., Yozwiak, C. E., Hoffstrom, B. G., Decker, A. M., Rajbhandari, P., Stokes, M. E., Bender, H. G., Csuka, J. M., Upadhyayula, P. S., Canoll, P., Uchida, K., Soni, R. K., Hadian, K., & Stockwell, B. R. (2020). Transferrin Receptor Is a Specific Ferroptosis Marker. *Cell Reports*, *30*(10), 3411-3423.e7. https://doi.org/10.1016/j.celrep.2020.02.049

Friedmann Angeli, J. P., Krysko, D. V., & Conrad, M. (2019). Ferroptosis at the crossroads of cancer-acquired drug resistance and immune evasion. *Nature Reviews Cancer*, *19*(7), Article 7. https://doi.org/10.1038/s41568-019-0149-1

Friedmann Angeli, J. P., Schneider, M., Proneth, B., Tyurina, Y. Y., Tyurin, V. A., Hammond, V. J., Herbach, N., Aichler, M., Walch, A., Eggenhofer, E., Basavarajappa, D., Rådmark, O., Kobayashi, S., Seibt, T., Beck, H., Neff, F., Esposito, I., Wanke, R., Förster, H., … Conrad, M. (2014). Inactivation of the ferroptosis regulator Gpx4 triggers acute renal failure in mice. *Nature Cell Biology*, *16*(12), Article 12. https://doi.org/10.1038/ncb3064

Galluzzi, L., Vitale, I., Aaronson, S. A., Abrams, J. M., Adam, D., Agostinis, P., Alnemri, E. S., Altucci, L., Amelio, I., Andrews, D. W., Annicchiarico-Petruzzelli, M., Antonov, A. V., Arama, E., Baehrecke, E. H., Barlev, N. A., Bazan, N. G., Bernassola, F., Bertrand, M. J. M., Bianchi, K., … Kroemer, G. (2018). Molecular mechanisms of cell death: Recommendations of the Nomenclature Committee on Cell Death 2018. *Cell Death & Differentiation*, *25*(3), Article 3. https://doi.org/10.1038/s41418-017-0012-4

Gao, M., Monian, P., Quadri, N., Ramasamy, R., & Jiang, X. (2015). Glutaminolysis and Transferrin Regulate Ferroptosis. *Molecular Cell*, *59*(2), 298–308. https://doi.org/10.1016/j.molcel.2015.06.011

Gaschler, M. M., & Stockwell, B. R. (2017). Lipid peroxidation in cell death. *Biochemical and Biophysical Research Communications*, *482*(3), 419–425. https://doi.org/10.1016/j.bbrc.2016.10.086

Hadian, K., & Stockwell, B. R. (2023). The therapeutic potential of targeting regulated non-apoptotic cell death. *Nature Reviews Drug Discovery*, *22*(9), Article 9. https://doi.org/10.1038/s41573-023-00749-8

Hambright, W. S., Fonseca, R. S., Chen, L., Na, R., & Ran, Q. (2017). Ablation of ferroptosis regulator glutathione peroxidase 4 in forebrain neurons promotes cognitive impairment and neurodegeneration. *Redox Biology*, *12*, 8–17. https://doi.org/10.1016/j.redox.2017.01.021

Hanahan, D., & Weinberg, R. A. (2000). The Hallmarks of Cancer. *Cell*, *100*(1), 57–70. https://doi.org/10.1016/S0092-8674(00)81683-9

Harterink, M., Port, F., Lorenowicz, M. J., McGough, I. J., Silhankova, M., Betist, M. C., van Weering, J. R. T., van Heesbeen, R. G. H. P., Middelkoop, T. C., Basler, K., Cullen, P. J., & Korswagen, H. C. (2011). A SNX3-dependent retromer pathway mediates retrograde transport of the Wnt sorting receptor Wntless and is required for Wnt secretion. *Nature Cell Biology*, *13*(8), Article 8. https://doi.org/10.1038/ncb2281

Hashidate-Yoshida, T., Harayama, T., Hishikawa, D., Morimoto, R., Hamano, F., Tokuoka, S. M., Eto, M., Tamura-Nakano, M., Yanobu-Takanashi, R.,

Mukumoto, Y., Kiyonari, H., Okamura, T., Kita, Y., Shindou, H., & Shimizu, T. (2015). Fatty acid remodeling by LPCAT3 enriches arachidonate in phospholipid membranes and regulates triglyceride transport. *eLife*, *4*, e06328. https://doi.org/10.7554/eLife.06328

Hino, K., Yanatori, I., Hara, Y., & Nishina, S. (2022). Iron and liver cancer: An inseparable connection. *The FEBS Journal*, *289*(24), 7810–7829. https://doi.org/10.1111/febs.16208

Hou, W., Xie, Y., Song, X., Sun, X., Lotze, M. T., Zeh, H. J., Kang, R., & Tang, D. (2016). Autophagy promotes ferroptosis by degradation of ferritin. *Autophagy*, *12*(8), 1425–1428. https://doi.org/10.1080/15548627.2016.1187366

Kagan, V. E., Mao, G., Qu, F., Angeli, J. P. F., Doll, S., Croix, C. S., Dar, H. H., Liu, B., Tyurin, V. A., Ritov, V. B., Kapralov, A. A., Amoscato, A. A., Jiang, J., Anthonymuthu, T., Mohammadyani, D., Yang, Q., Proneth, B., Klein-Seetharaman, J., Watkins, S., … Bayır, H. (2017). Oxidized arachidonic and adrenic PEs navigate cells to ferroptosis. *Nature Chemical Biology*, *13*(1), Article 1. https://doi.org/10.1038/nchembio.2238

Karlsson, M., Zhang, C., Méar, L., Zhong, W., Digre, A., Katona, B., Sjöstedt, E., Butler, L., Odeberg, J., Dusart, P., Edfors, F., Oksvold, P., von Feilitzen, K., Zwahlen, M., Arif, M., Altay, O., Li, X., Ozcan, M., Mardinoglu, A., … Lindskog, C. (2021). A single–cell type transcriptomics map of human tissues. *Science Advances*, *7*(31), eabh2169. https://doi.org/10.1126/sciadv.abh2169

Kerr, J. F. R., Wyllie, A. H., & Currie, A. R. (1972). Apoptosis: A Basic Biological Phenomenon with Wideranging Implications in Tissue Kinetics. *British Journal of Cancer*, *26*(4), Article 4. https://doi.org/10.1038/bjc.1972.33

Kühn, H., & Borchert, A. (2002). Regulation of enzymatic lipid peroxidation: The interplay of peroxidizing and peroxide reducing enzymes1 1This article is part of a series of reviews on “Regulatory and Cytoprotective Aspects of Lipid Hydroperoxide Metabolism.” The full list of papers may be found on the homepage of the journal. *Free Radical Biology and Medicine*, *33*(2), 154–172. https://doi.org/10.1016/S0891-5849(02)00855-9

Kuwata, H., Nakatani, E., Shimbara-Matsubayashi, S., Ishikawa, F., Shibanuma, M., Sasaki, Y., Yoda, E., Nakatani, Y., & Hara, S. (2019). Long-chain acyl-CoA synthetase 4 participates in the formation of highly unsaturated fatty acid-containing phospholipids in murine macrophages. *Biochimica et Biophysica Acta (BBA) - Molecular and Cell Biology of Lipids*, *1864*(11), 1606–1618. https://doi.org/10.1016/j.bbalip.2019.07.013

Lei, G., Zhuang, L., & Gan, B. (2022). Targeting ferroptosis as a vulnerability in cancer. *Nature Reviews Cancer*, *22*(7), Article 7. https://doi.org/10.1038/s41568-022-00459-0

Leneva, N., Kovtun, O., Morado, D. R., Briggs, J. A. G., & Owen, D. J. (2021). Architecture and mechanism of metazoan retromer:SNX3 tubular coat assembly. *Science Advances*, *7*(13), eabf8598. https://doi.org/10.1126/sciadv.abf8598

Li, L., Hao, Y., Zhao, Y., Wang, H., Zhao, X., Jiang, Y., & Gao, F. (2018). Ferroptosis is associated with oxygen-glucose deprivation/reoxygenation-induced Sertoli cell death. *International Journal of Molecular Medicine*, *41*(5), 3051–3062. https://doi.org/10.3892/ijmm.2018.3469

Li, M., Wang, X., Lu, S., He, C., Wang, C., Wang, L., Wang, X., Ge, P., & Song, D. (2020). Erastin triggers autophagic death of breast cancer cells by increasing intracellular iron levels. *Oncology Letters*, *20*(4), 1–1. https://doi.org/10.3892/ol.2020.11918

Li, P., Jiang, M., Li, K., Li, H., Zhou, Y., Xiao, X., Xu, Y., Krishfield, S., Lipsky, P. E., Tsokos, G. C., & Zhang, X. (2021). Glutathione peroxidase 4–regulated neutrophil ferroptosis induces systemic autoimmunity. *Nature Immunology*, *22*(9), Article 9. https://doi.org/10.1038/s41590-021-00993-3

Liu, L., & Kang, X. (2022). ACSL4 is overexpressed in psoriasis and enhances inflammatory responses by activating ferroptosis. *Biochemical and Biophysical Research Communications*, *623*, 1–8. https://doi.org/10.1016/j.bbrc.2022.07.041

Liu, X., Taftaf, R., Kawaguchi, M., Chang, Y.-F., Chen, W., Entenberg, D., Zhang, Y.,

Gerratana, L., Huang, S., Patel, D. B., Tsui, E., Adorno-Cruz, V., Chirieleison, S. M., Cao, Y., Harney, A. S., Patel, S., Patsialou, A., Shen, Y., Avril, S., … Liu, H. (2019). Homophilic CD44 Interactions Mediate Tumor Cell Aggregation and Polyclonal Metastasis in Patient-Derived Breast Cancer Models. *Cancer Discovery*, *9*(1), 96–113. https://doi.org/10.1158/2159-8290.CD-18-0065

Lucas, M., Gershlick, D. C., Vidaurrazaga, A., Rojas, A. L., Bonifacino, J. S., & Hierro, A. (2016). Structural Mechanism for Cargo Recognition by the Retromer Complex. *Cell*, *167*(6), 1623-1635.e14. https://doi.org/10.1016/j.cell.2016.10.056

Lyamzaev, K. G., Panteleeva, A. A., Simonyan, R. A., Avetisyan, A. V., & Chernyak, B. V. (2023). Mitochondrial Lipid Peroxidation Is Responsible for Ferroptosis. *Cells*, *12*(4), Article 4. https://doi.org/10.3390/cells12040611

Mancias, J. D., Wang, X., Gygi, S. P., Harper, J. W., & Kimmelman, A. C. (2014). Quantitative proteomics identifies NCOA4 as the cargo receptor mediating ferritinophagy. *Nature*, *509*(7498), Article 7498. https://doi.org/10.1038/nature13148

Martinez, A. M., Kim, A., & Yang, W. S. (2020). Detection of Ferroptosis by BODIPY™ 581/591 C11. In I. Vancurova & Y. Zhu (Eds.), *Immune Mediators in Cancer: Methods and Protocols* (pp. 125–130). Springer US. https://doi.org/10.1007/978-1-0716-0247-8_11

Miao, Z., Tian, W., Ye, Y., Gu, W., Bao, Z., Xu, L., Sun, G., Li, C., Tu, Y., Chao, H., Lam, S. M., Liu, N., & Ji, J. (2022). Hsp90 induces Acsl4-dependent glioma ferroptosis via dephosphorylating Ser637 at Drp1. *Cell Death & Disease*, *13*(6), Article 6. https://doi.org/10.1038/s41419-022-04997-1

Moreno, P., Fexova, S., George, N., Manning, J. R., Miao, Z., Mohammed, S., Muñoz-Pomer, A., Fullgrabe, A., Bi, Y., Bush, N., Iqbal, H., Kumbham, U., Solovyev, A., Zhao, L., Prakash, A., García-Seisdedos, D., Kundu, D. J., Wang, S., Walzer, M., … Papatheodorou, I. (2022). Expression Atlas update: Gene and protein expression in multiple species. *Nucleic Acids Research*, *50*(D1), D129–D140. https://doi.org/10.1093/nar/gkab1030

Müller, S., Sindikubwabo, F., Cañeque, T., Lafon, A., Versini, A., Lombard, B., Loew, D., Wu, T.-D., Ginestier, C., Charafe-Jauffret, E., Durand, A., Vallot, C., Baulande, S., Servant, N., & Rodriguez, R. (2020). CD44 regulates epigenetic plasticity by mediating iron endocytosis. *Nature Chemistry*, *12*(10), Article 10. https://doi.org/10.1038/s41557-020-0513-5

Ohgami, R. S., Campagna, D. R., Greer, E. L., Antiochos, B., McDonald, A., Chen, J., Sharp, J. J., Fujiwara, Y., Barker, J. E., & Fleming, M. D. (2005). Identification of a ferrireductase required for efficient transferrin-dependent iron uptake in erythroid cells. *Nature Genetics*, *37*(11), Article 11. https://doi.org/10.1038/ng1658

Öyken, M. (2020). *Characterization of sorting nexin 3 (SNX3) function*. https://open.metu.edu.tr/handle/11511/45332

Pinnix, Z. K., Miller, L. D., Wang, W., D'Agostino, R., Kute, T., Willingham, M. C., Hatcher, H., Tesfay, L., Sui, G., Di, X., Torti, S. V., & Torti, F. M. (2010). Ferroportin and Iron Regulation in Breast Cancer Progression and Prognosis. *Science Translational Medicine*, *2*(43), 43ra56-43ra56. https://doi.org/10.1126/scitranslmed.3001127

Qu, X., Liang, T., Wu, D., Lai, N., Deng, R., Ma, C., Li, X., Li, H., Liu, Y., Shen, H., & Chen, G. (2021). Acyl-CoA synthetase long chain family member 4 plays detrimental role in early brain injury after subarachnoid hemorrhage in rats by inducing ferroptosis. *CNS Neuroscience & Therapeutics*, *27*(4), 449–463. https://doi.org/10.1111/cns.13548

Reed, A., Ichu, T.-A., Milosevich, N., Melillo, B., Schafroth, M. A., Otsuka, Y., Scampavia, L., Spicer, T. P., & Cravatt, B. F. (2022). LPCAT3 Inhibitors Remodel the Polyunsaturated Phospholipid Content of Human Cells and Protect from Ferroptosis. *ACS Chemical Biology*, *17*(6), 1607–1618. https://doi.org/10.1021/acschembio.2c00317

Sato, H., Tamba, M., Ishii, T., & Bannai, S. (1999). Cloning and Expression of a Plasma Membrane Cystine/Glutamate Exchange Transporter Composed of Two Distinct Proteins*. *Journal of Biological Chemistry*, *274*(17), 11455–11458. https://doi.org/10.1074/jbc.274.17.11455

Seiler, A., Schneider, M., Förster, H., Roth, S., Wirth, E. K., Culmsee, C., Plesnila, N., Kremmer, E., Rådmark, O., Wurst, W., Bornkamm, G. W., Schweizer, U., & Conrad, M. (2008). Glutathione Peroxidase 4 Senses and Translates Oxidative Stress into 12/15-Lipoxygenase Dependent- and AIF-Mediated Cell Death. *Cell Metabolism*, *8*(3), 237–248. https://doi.org/10.1016/j.cmet.2008.07.005

Shah, R., Shchepinov, M. S., & Pratt, D. A. (2018). Resolving the Role of Lipoxygenases in the Initiation and Execution of Ferroptosis. *ACS Central Science*, *4*(3), 387–396. https://doi.org/10.1021/acscentsci.7b00589

Skouta, R., Dixon, S. J., Wang, J., Dunn, D. E., Orman, M., Shimada, K., Rosenberg, P. A., Lo, D. C., Weinberg, J. M., Linkermann, A., & Stockwell, B. R. (2014). Ferrostatins Inhibit Oxidative Lipid Damage and Cell Death in Diverse Disease Models. *Journal of the American Chemical Society*, *136*(12), 4551–4556. https://doi.org/10.1021/ja411006a

Stockwell, B. R. (2022). Ferroptosis turns 10: Emerging mechanisms, physiological functions, and therapeutic applications. *Cell*, *185*(14), 2401–2421. https://doi.org/10.1016/j.cell.2022.06.003

Sun, W.-Y., Tyurin, V. A., Mikulska-Ruminska, K., Shrivastava, I. H., Anthonymuthu, T. S., Zhai, Y.-J., Pan, M.-H., Gong, H.-B., Lu, D.-H., Sun, J., Duan, W.-J., Korolev, S., Abramov, A. Y., Angelova, P. R., Miller, I., Beharier, O., Mao, G.-W., Dar, H. H., Kapralov, A. A., … Kagan, V. E. (2021). Phospholipase iPLA2β averts ferroptosis by eliminating a redox lipid death signal. *Nature Chemical Biology*, *17*(4), Article 4. https://doi.org/10.1038/s41589-020-00734-x

Ubellacker, J. M., Tasdogan, A., Ramesh, V., Shen, B., Mitchell, E. C., Martin-Sandoval, M. S., Gu, Z., McCormick, M. L., Durham, A. B., Spitz, D. R., Zhao, Z., Mathews, T. P., & Morrison, S. J. (2020). Lymph protects metastasizing melanoma cells from ferroptosis. *Nature*, *585*(7823), Article 7823. https://doi.org/10.1038/s41586-020-2623-z

Van San, E., Debruyne, A. C., Veeckmans, G., Tyurina, Y. Y., Tyurin, V. A., Zheng, H., Choi, S. M., Augustyns, K., van Loo, G., Michalke, B., Venkataramani, V.,

Toyokuni, S., Bayir, H., Vandenabeele, P., Hassannia, B., & Vanden Berghe, T. (2023). Ferroptosis contributes to multiple sclerosis and its pharmacological targeting suppresses experimental disease progression. *Cell Death & Differentiation*, *30*(9), Article 9. https://doi.org/10.1038/s41418-023-01195-0

Viswanathan, V. S., Ryan, M. J., Dhruv, H. D., Gill, S., Eichhoff, O. M., Seashore-Ludlow, B., Kaffenberger, S. D., Eaton, J. K., Shimada, K., Aguirre, A. J., Viswanathan, S. R., Chattopadhyay, S., Tamayo, P., Yang, W. S., Rees, M. G., Chen, S., Boskovic, Z. V., Javaid, S., Huang, C., … Schreiber, S. L. (2017). Dependency of a therapy-resistant state of cancer cells on a lipid peroxidase pathway. *Nature*, *547*(7664), Article 7664. https://doi.org/10.1038/nature23007

Walter, R. J., Sonnentag, S. J., Munoz-Sagredo, L., Merkel, M., Richert, L., Bunert, F., Heneka, Y. M., Loustau, T., Hodder, M., Ridgway, R. A., Sansom, O. J., Mely, Y., Rothbauer, U., Schmitt, M., & Orian-Rousseau, V. (2022). Wnt signaling is boosted during intestinal regeneration by a CD44-positive feedback loop. *Cell Death & Disease*, *13*(2), Article 2. https://doi.org/10.1038/s41419-022-04607-0

Wang, D., Liang, W., Huo, D., Wang, H., Wang, Y., Cong, C., Zhang, C., Yan, S., Gao, M., Su, X., Tan, X., Zhang, W., Han, L., Zhang, D., & Feng, H. (2023). SPY1 inhibits neuronal ferroptosis in amyotrophic lateral sclerosis by reducing lipid peroxidation through regulation of GCH1 and TFR1. *Cell Death & Differentiation*, *30*(2), Article 2. https://doi.org/10.1038/s41418-022-01089-7

Wang, H., Wang, P., & Zhu, B. T. (2022). Mechanism of Erastin-Induced Ferroptosis in MDA-MB-231 Human Breast Cancer Cells: Evidence for a Critical Role of Protein Disulfide Isomerase. *Molecular and Cellular Biology*, *42*(6), e00522-21. https://doi.org/10.1128/mcb.00522-21

Wang, T., Tomas, D., Perera, N. D., Cuic, B., Luikinga, S., Viden, A., Barton, S. K., McLean, C. A., Samson, A. L., Southon, A., Bush, A. I., Murphy, J. M., & Turner, B. J. (2022). Ferroptosis mediates selective motor neuron death in amyotrophic lateral sclerosis. *Cell Death & Differentiation*, *29*(6), Article 6. https://doi.org/10.1038/s41418-021-00910-z

Wu, H., & Liu, A. (2021). Long non-coding RNA NEAT1 regulates ferroptosis sensitivity in non-small-cell lung cancer. *Journal of International Medical Research*, *49*(3), 0300060521996183. https://doi.org/10.1177/0300060521996183

Yang, W. S., Kim, K. J., Gaschler, M. M., Patel, M., Shchepinov, M. S., & Stockwell, B. R. (2016). Peroxidation of polyunsaturated fatty acids by lipoxygenases drives ferroptosis. *Proceedings of the National Academy of Sciences*, *113*(34), E4966–E4975. https://doi.org/10.1073/pnas.1603244113

Yang, W. S., SriRamaratnam, R., Welsch, M. E., Shimada, K., Skouta, R., Viswanathan, V. S., Cheah, J. H., Clemons, P. A., Shamji, A. F., Clish, C. B., Brown, L. M., Girotti, A. W., Cornish, V. W., Schreiber, S. L., & Stockwell, B. R. (2014). Regulation of Ferroptotic Cancer Cell Death by GPX4. *Cell*, *156*(1), 317–331. https://doi.org/10.1016/j.cell.2013.12.010

Yang, Y., Lin, Y., Wang, M., Yuan, K., Wang, Q., Mu, P., Du, J., Yu, Z., Yang, S., Huang, K., Wang, Y., Li, H., & Tang, T. (2022). Targeting ferroptosis suppresses osteocyte glucolipotoxicity and alleviates diabetic osteoporosis. *Bone Research*, *10*(1), Article 1. https://doi.org/10.1038/s41413-022-00198-w

Yi, J., Zhu, J., Wu, J., Thompson, C. B., & Jiang, X. (2020). Oncogenic activation of PI3K-AKT-mTOR signaling suppresses ferroptosis via SREBP-mediated lipogenesis. *Proceedings of the National Academy of Sciences*, *117*(49), 31189–31197. https://doi.org/10.1073/pnas.2017152117

Yu, W., Hu, Y., Liu, Z., Guo, K., Ma, D., Peng, M., Wang, Y., Zhang, J., Zhang, X., Wang, P., Zhang, J., Liu, P., & Lu, J. (2023). Sorting nexin 3 exacerbates doxorubicin-induced cardiomyopathy via regulation of TFRC-dependent ferroptosis. *Acta Pharmaceutica Sinica B*. https://doi.org/10.1016/j.apsb.2023.08.016

Zhang, H.-L., Hu, B.-X., Li, Z.-L., Du, T., Shan, J.-L., Ye, Z.-P., Peng, X.-D., Li, X., Huang, Y., Zhu, X.-Y., Chen, Y.-H., Feng, G.-K., Yang, D., Deng, R., & Zhu, X.-F. (2022). PKCβII phosphorylates ACSL4 to amplify lipid peroxidation to induce ferroptosis. *Nature Cell Biology*, *24*(1), Article 1. https://doi.org/10.1038/s41556-021-00818-3

Appendix

Figure 1. Test for normal distribution for the RT-qPCR data

	HeLa	MDA-MB-436	MDA-MB-231	MDA-MB-468	MCF-7
Test for normal distribution					
Shapiro-Wilk test					
W	0,9802	0,9663	0,932	0,923	0,8772
P value	0,9651	0,8613	0,537	0,4177	0,1771
Passed normality test (alpha=0.05)?	Yes	Yes	Yes	Yes	Yes
P value summary	ns	ns	ns	ns	ns
Kolmogorov-Smirnov test					
KS distance	0,1718	0,1792	0,1558	0,2032	0,1981
P value	>0,1000	>0,1000	>0,1000	>0,1000	>0,1000
Passed normality test (alpha=0.05)?	Yes	Yes	Yes	Yes	Yes
P value summary	ns	ns	ns	ns	ns
Number of values	9	9	8	9	8

Figure 2. Results of ordinary one-way ANOVA for the RT-qPCR data

ANOVA summary	
F	6,287
P value	0,0006
P value summary	***
Significant diff. among means (P < 0.05)?	Yes
R square	0,3982

Figure 3. Tukey's multiple comparisons test for the RT-qPCR data

Tukey's multiple comparisons test	Mean Diff,	95,00% CI of diff,	Significant?	Summary	Adjusted P Value	
HeLa vs. MDA-MB-436	-0,3869	-0,6425 to -0,1313	Yes	***	0,0009	A-B
HeLa vs. MDA-MB-231	-0,2201	-0,4836 to 0,04337	No	ns	0,1397	A-C
HeLa vs. MDA-MB-468	-0,354	-0,6096 to -0,09841	Yes	**	0,0027	A-D
HeLa vs. MCF-7	-0,3438	-0,6073 to -0,08036	Yes	**	0,0052	A-E
MDA-MB-436 vs. MDA-MB-231	0,1668	-0,09663 to 0,4303	No	ns	0,3813	B-C
MDA-MB-436 vs. MDA-MB-468	0,03293	-0,2227 to 0,2885	No	ns	0,9959	B-D
MDA-MB-436 vs. MCF-7	0,04311	-0,2204 to 0,3066	No	ns	0,9897	B-E
MDA-MB-231 vs. MDA-MB-468	-0,1339	-0,3974 to 0,1296	No	ns	0,5969	C-D
MDA-MB-231 vs. MCF-7	-0,1237	-0,3948 to 0,1474	No	ns	0,6888	C-E
MDA-MB-468 vs. MCF-7	0,01018	-0,2533 to 0,2737	No	ns	>0,9999	D-E

Figure 4. Normal QQ plot for the RT-qPCR data

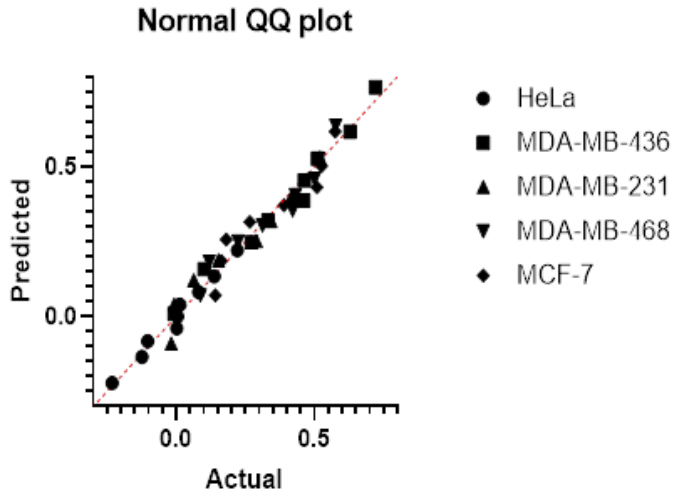

Figure 5. Normality test for the Alamar blue cell viability assay

	NT	E 2,5mkM	E 5mkM	E 10mkM	E 20mkM	DMSO
Shapiro-Wilk test						
W	0,9320	0,9412	0,9631	0,9348	0,9679	0,7981
P value	0,5683	0,6230	0,8395	0,5926	0,8783	0,0989
Passed normality test (alpha=0.05)?	Yes	Yes	Yes	Yes	Yes	Yes
P value summary	ns	ns	ns	ns	ns	ns

Figure 6. Results of ordinary one-way ANOVA for the Alamar blue cell viability assay

ANOVA summary	
F	41,34
P value	<0,0001
P value summary	****
Significant diff. among means (P < 0.05)?	Yes
R square	0,8588

Figure 7. Tukey's multiple comparisons test for the Alamar blue cell viability assay

Tukey's multiple comparisons test	Significant?	Summary	Adjusted P Value
NT vs. E 2,5mkM	Yes	***	0,0002
NT vs. E 5mkM	Yes	****	<0,0001
NT vs. E 10mkM	Yes	****	<0,0001
NT vs. E 20mkM	Yes	****	<0,0001
NT vs. DMSO	Yes	**	0,005
E 2,5mkM vs. E 5mkM	No	ns	0,6329
E 2,5mkM vs. E 10mkM	Yes	****	<0,0001
E 2,5mkM vs. E 20mkM	Yes	****	<0,0001
E 2,5mkM vs. DMSO	No	ns	0,9998
E 5mkM vs. E 10mkM	Yes	**	0,0025
E 5mkM vs. E 20mkM	Yes	****	<0,0001
E 5mkM vs. DMSO	No	ns	0,6453
E 10mkM vs. E 20mkM	No	ns	0,0684
E 10mkM vs. DMSO	Yes	***	0,0003
E 20mkM vs. DMSO	Yes	****	<0,0001

Figure 8. Normal QQ plot for the Alamar blue cell viability assay

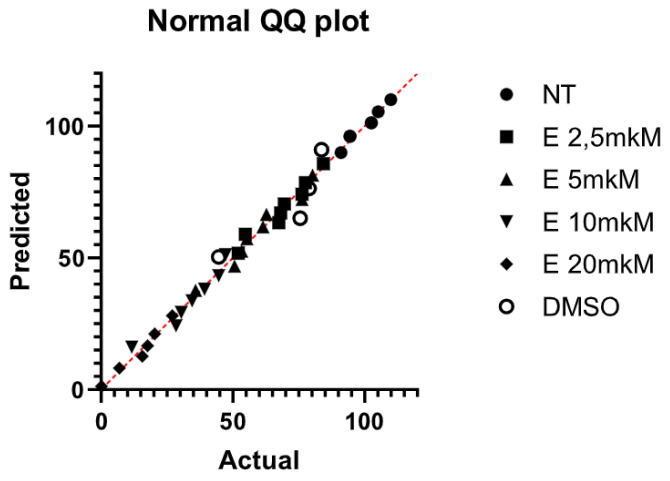

Figure 9. Effects of 2.5 uM and 5 uM erastin treatment on the morphology of MDA-MB-231 cells.

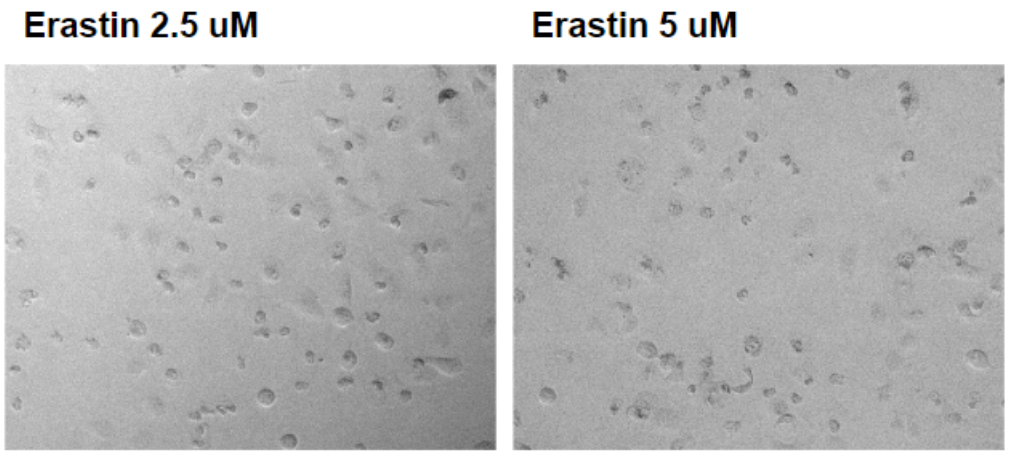

Figure 10. Effects of 10 uM and 15 uM erastin treatment with 2.5 uM Fer-1 pre-treatment on the morphology of MDA-MB-231 cells.

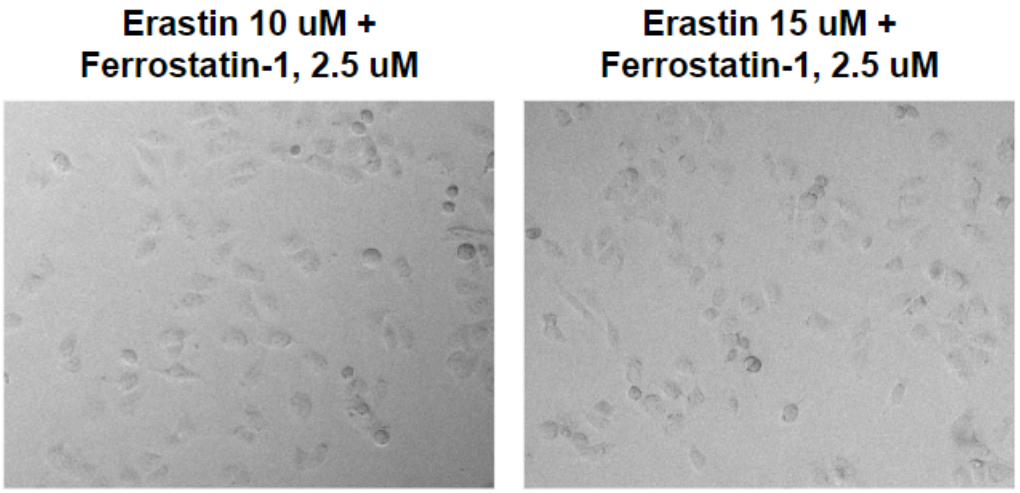

Figure 11. Flow cytometry density plots showing the effects of 2.5 uM, 5 uM, and 15 uM erastin treatment on MDA-MB-231 cells

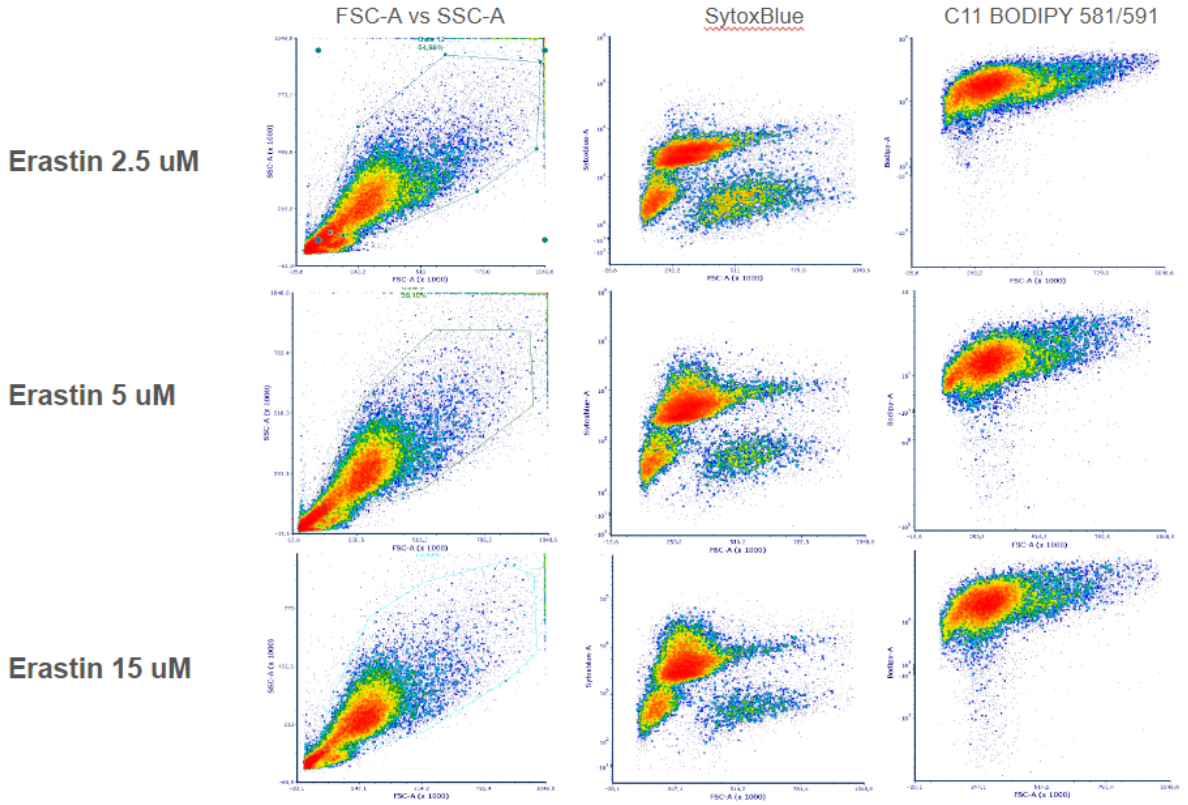

Figure 12. Flow cytometry density plots showing the effects of 5 uM and 15 uM erastin treatment with 5 uM Fer-1 pre-treatment on MDA-MB-231 cells

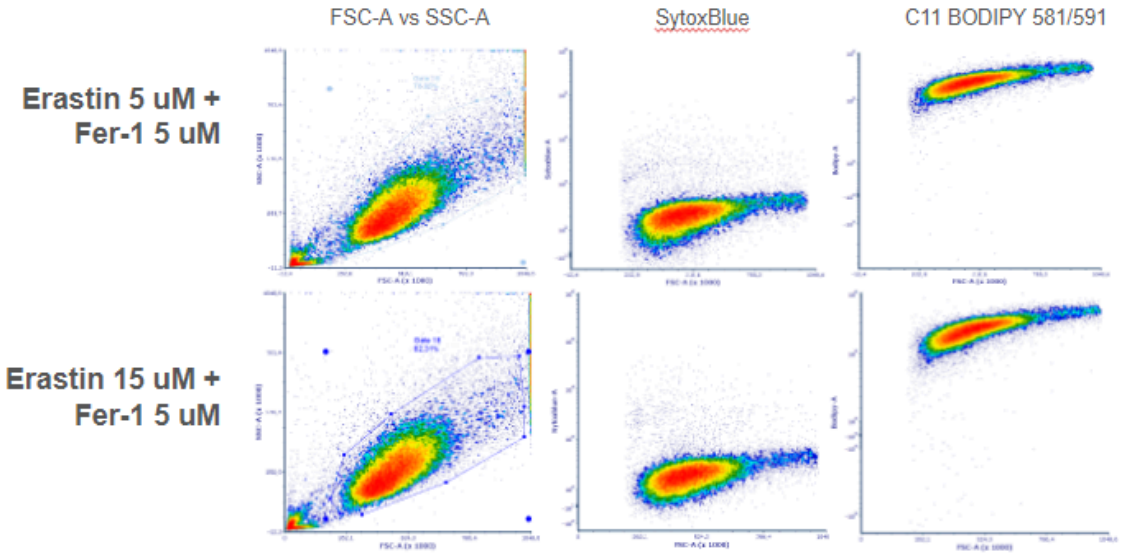

Figure 13. Map of the SNX3-pEGFP plasmid. The map was visualized using SnapGene Viewer.

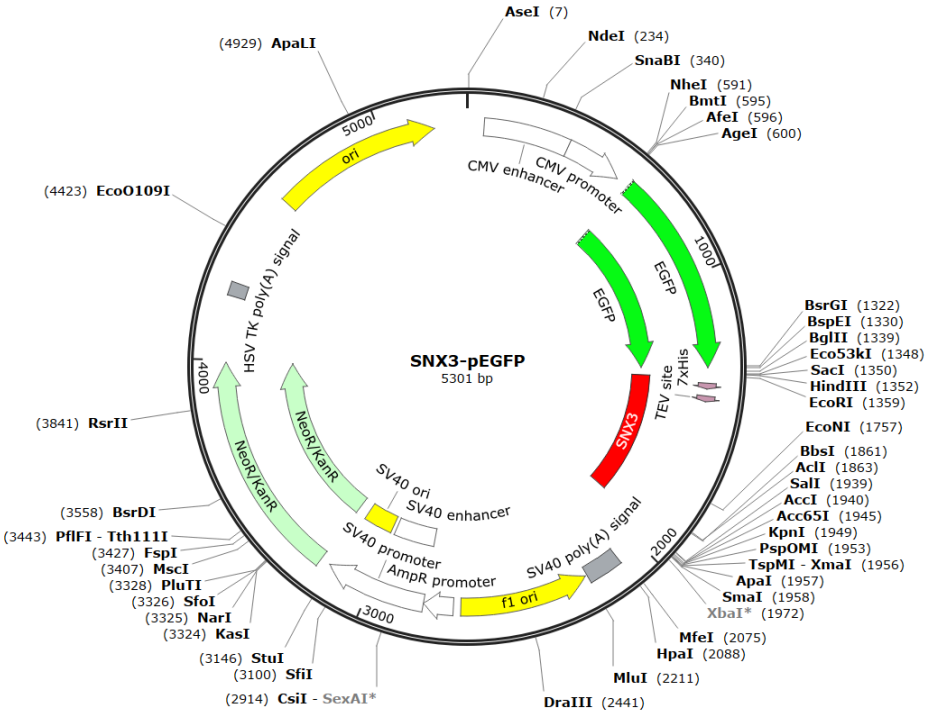

Figure 14. Manufacturer's image of SNX3 fluorescence (green color) using the Anti-SNX3 (ab56078) primary antibody. Nucleus was countersained with DAPI (blue). Red is tubulin.

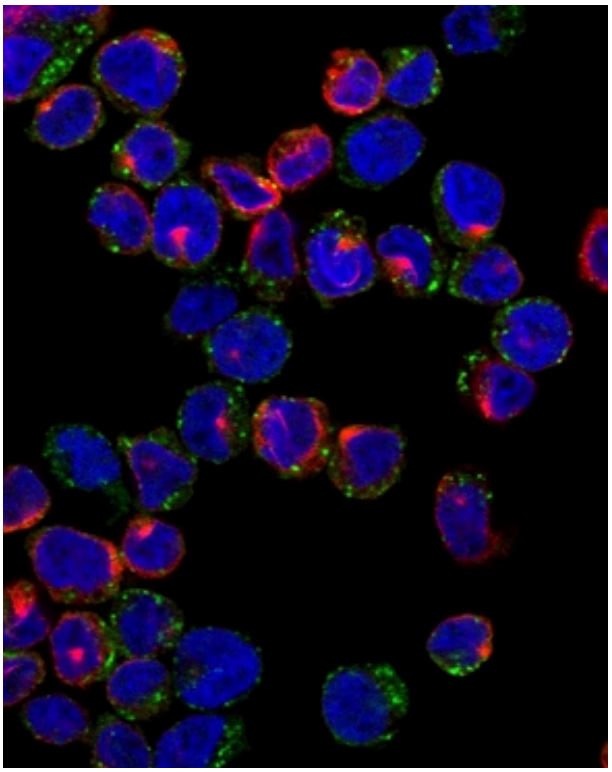

Figure 15. gRNA1-transfected cell imaged for SNX3. SNX3 was labelled with Anti-SNX3 (ab56078) primary antibody and AlexaFluor 647-conjugated secondary antibody

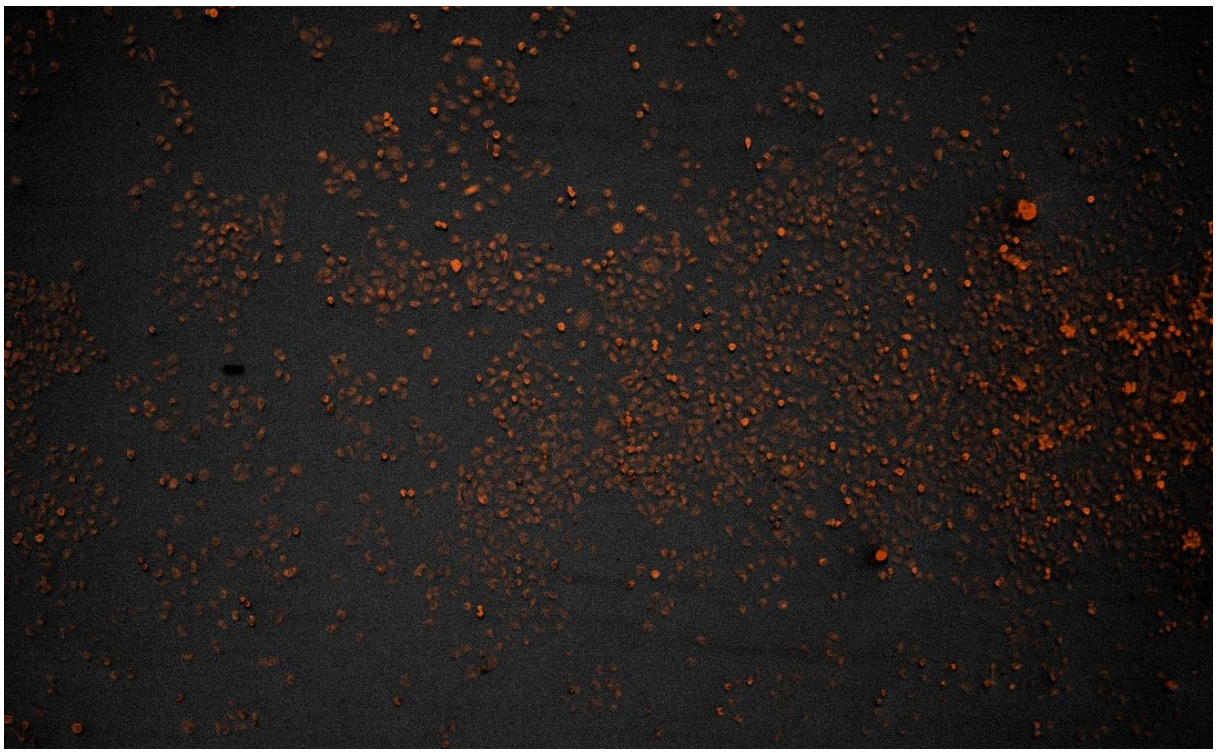

Figure 16. Z-stack through the nucleus of wild-type MDA-MB-231 cells labelled with Anti-TFRC (ab193188) primary antibody (red).

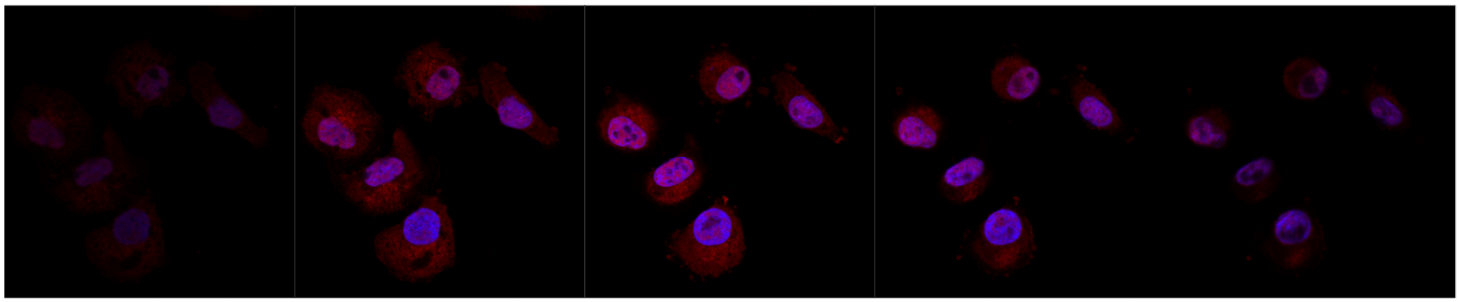

Figure 17. Manufacturer's image of TFRC fluorescence (green color) using the Anti-TFRC (ab56078) primary antibody. Nucleus was countersained with DAPI (blue).

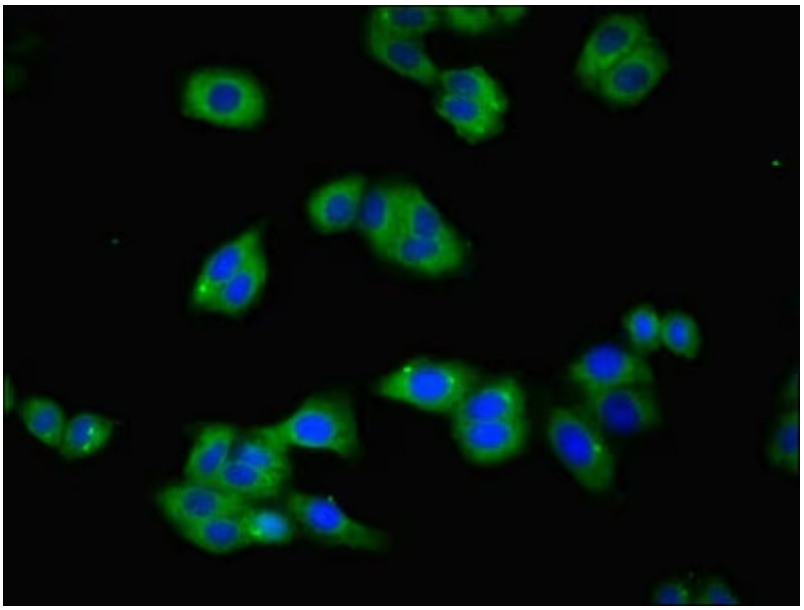

Figure 18. Sequences of primer used for RT-qPCR

Name	5' to 3' Sequence
SNX3 FP	AAGAGAGAGCAAGGGTCGCTG
SNX3 RP	CACGTTTTTGCCCCTTCTTGC
GAPDH2 FP	ACCACAGTCCATGCCATCA
GAPDH2 RP	CCACCACCCTGTTGCTGT

Figure 19. Sequences of primers used for genomic PCR

Name	5' to 3' Sequence
3F	CCTATGACCGAGTACAAGCCC
3R	GAAGTCAACCATGTCCAATCAC
5F	CTAAAGCCGTTTCCGGCGCTCTA
5R	CAGGTGGAAGTAATTCAAGGCAC